Flares in Open Clusters with K2.

II. Pleiades, Hyades, Praesepe, Ruprecht 147, and M67

Ekaterina Ilin[1], Sarah J. Schmidt[1], Katja Poppenhäger[1], James R. A. Davenport[2] and Klaus G. Strassmeier[1]

[1] Leinbiz Institut für Astrophysik Potsdam
  e-mail: eilin@aip.de
[2] University of Washington e-mail: jrad@uw.edu

ABSTRACT

Context. Flares can help us trace magnetic activity because they are bright and high-contrast on low mass stars.
Aims. This study aims to quantify flaring activity on these stars as a function of mass and age.
Methods. We searched the light curves of open cluster stars in K2 time-domain photometry for flares using the open-source software packages K2SC and AltaiPony. K2SC was used to remove instrumental and astrophysical variability from K2 light curves, and AltaiPony to search and characterize the flare candidates. With the full K2 archive we added stars with a larger variety of ages and spectral types to the analysis of the previous study (Ilin et al. 2019) and manually confirmed a total of 2913 flares. We compared previous results from Prasepe to the flare frequency distributions (FFDs) in the Hyades, respectively. Ruprecht 147 filled in the age gap at 2.5 Gyr between the aforementioned young clusters and the 3.6 Gyr old M67.
Results. We find that the flare production mechanism is similar for the entire parameter space, following a power law relation with exponent $\alpha \approx 1.9$, but the flaring frequencies depend on both mass, and age. We discuss X and Y.

Key words. Methods: data analysis, Stars: activity, Stars: flare, Stars: low-mass

Use \titlerunning to supply a shorter title and/or \authorrunning to supply a shorter list of authors.

1. Introduction

Flares are explosions on stellar surfaces with a complex spatio-temporal and energetic phenomenology. We know that flares are magnetic re-connection events that lead to a change in field line topology and subsequent energy release (Priest & Forbes 2002). We can observe flares in nearly all electromagnetic bands, from radio to X-rays, and on all stars that possess a convection zone, from late F type stars to ultracool dwarfs (Gizis 2013). But even with continuous monitoring at high temporal resolution, the random occurrence of solar flares makes them costly observing targets, especially in coordinated multi-band observations. In integrated light, most solar flares have a far too low contrast and intensity to be observable. Stellar flares on cool stars have two advantages in this respect. They are often bright, enhancing stellar flux by up to several orders of magnitude, and they typically exhibit blackbody emission at temperatures significantly higher than their stars' photospheres.

With the evidence that the physical processes that cause flares on the Sun and other stars are the same (Karoff 2016), solar and stellar flares can inform each other (Shibayama et al. 2013). Inconsistencies in extrapolations from solar to stellar conditions (Aarnio et al. 2011; Aarnio et al. 2012; Drake et al. 2013) provide valuable clues to the differences in magnetic properties between Sun and M dwarfs, too (Alvarado-Gómez et al. 2018). Large surveys like Kepler and TESS enable statistical flare studies of stars that were not pre-selected for their activity (Walkowicz et al. 2011). Statistical studies of stellar flaring activity can help us understand the underlying physical processes CITE stellar surface magnetic fields, starspots (Davenport 2015; Howard

et al. 2019b), how flares relate to stellar angular momentum evolution (Mondrik et al. 2019; Howard et al. 2019b), how they affect the atmospheres of exoplanets (Lecavelier des Etangs et al. 2012; Loyd et al. 2018; Tilley et al. 2019; Howard et al. 2019a), and inform galactic archaeology (Howard et al. 2019a).
Basic parameters that affect flaring behaviour on stars are their masses, and ages. Ages can be controlled for in coeval groups of stars, and flaring-age studies in binaries showed consistency in activity for both components in the majority of targets (Lurie et al. 2015; Clarke et al. 2018). Open clusters present other coeval groups of stars with well-determined ages. Ilin et al. (2019) (hereafter PaperI) investigated the flaring activity of late-K to mid-M dwarfs in three open clusters (OCs), the Pleiades, Praesepe, and M67, using K2 time domain photometry. They analysed the flare frequency distributions (FFDs), with respect to different masses and cluster ages. For the cluster members, the light curves revealed that their flaring activity declines both with age and mass. The decline is faster for higher mass stars. Recently, Davenport et al. (2019) put forward an empirical parametrization of this flaring-mass-age relation based on FFDs. The present study aims to extend the results in PaperI to the age of Ruprecht 147 (2.5 Gyr), and both higher and lower masses than in the previous study. We also test the previous results from the Pleiades on M35, and the results from Praesepe on the Hyades, as both OC pairs have approximately the same ages. Because the Kepler satellite retired in fall 2018, we can now use the complete K2 data set, and supplement all three OCs in PaperI with additional light curves. Additionally, we use high quality K2 light curves available for M67 (Nardiello et al. 2016) and M35 (Soares-Furtado et al. 2017). We discuss our results with
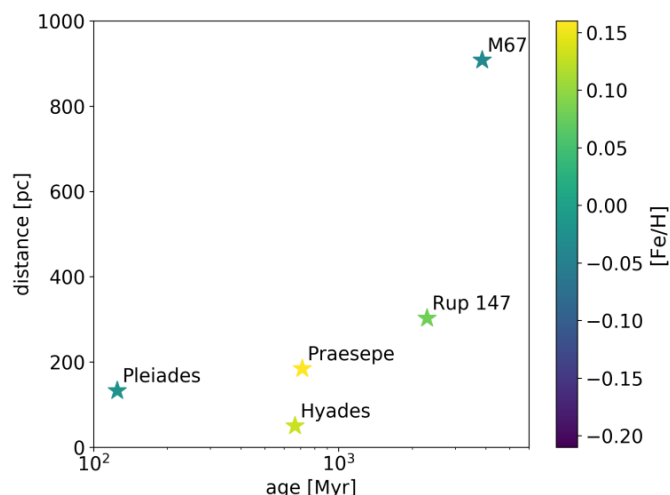
Fig. 1. The values for age, metallicity, and distance are approximate values from a compilation of existing literature, see Appendix B.1.

respect to potential breaks in the power law distribution at high energies. Finally, we use the results to test the parametrization in Davenport et al. (2019).

2. Data

Our main data are K2 target pixel files that were provided by the Kepler archives hosted at MAST, and light curves derived from them (Aigrain et al. 2016; Soares-Furtado et al. 2017; Vinícius et al. 2018). To assign T_{eff} to the targeted stars we used multi-band photometry obtained from Tycho, UCAC4, 2MASS, Pan-STARRS, and Gaia catalogs. To assign ages to the targeted stars, OC membership information was compiled from the literature. An overview over the cluster sample is presented in Table **??** and illustrated in Figure 1.

2.1. K2 light curves

The Kepler (Koch et al. 2010) spacecraft finished its follow-up mission K2 (Howell et al. 2014) in September 2018, after having completed nearly 20 80-day observing campaigns. Even thought Kepler and K2 data are used in more than 2 400 publications to date, the public archive can still considered understudied (Barentsen et al. 2018). In this spirit we took up the analysis of about 4 000 Kepler target pixel files that each contain up 80 days of 30 min cadence observations in white light $(4, 200 - 9, 000 \text{Å})$. We also used light curves extracted from the K2 C0 super stamp. A super stamp is an aggregated set of typical Kepler postage stamps placed over a densely populated field, that also covered M35 (Soares-Furtado et al. 2017).

As K2 was conducted on the two-wheeled Kepler satellite, it was subjected to substantial drift motion (spacecraft roll, Van Cleve et al. 2016) and had an overall reduced pointing accuracy. To mitigate these effects, various solutions were developed (Vanderburg & Johnson 2014; Aigrain et al. 2016; **?**; Luger et al. 2018)

2.2. Membership matching

We obtained membership information from multiple catalogs for each cluster. We cross-matched these catalogs on RA and

declination within 3 arcsec. The resulting target lists were used to search the K2 archive, or were matched to the catalogs of extracted light curves from crowded fields in the case of M35 (Soares-Furtado et al. 2017) and M67 (Nardiello et al. 2016).

One part of the membership catalogs provided membership probabilities (Douglas et al. 2014; Bouy et al. 2015; Cantat-Gaudin et al. 2018; Olivares et al. 2018; Reino et al. 2018; Gao 2018; Olivares et al. 2019). For the other part no probability was provided (Rebull et al. 2016a; Douglas et al. 2017; Gaia Collaboration et al. 2018a), or qualitative classifiers were given (Curtis et al. 2013; Gonzalez 2016; Rebull et al. 2017). In the latter cases we assigned approximate probabilities anchored to the set threshold for inclusion into our final sample. Absence in a catalog did not decrease the likelihood of membership, as each catalog shows different selection biases which we did not address in this study. We set the threshold mean membership probability p for a target in our sample to 0.8.

2.3. Open Clusters

We studied flaring activity in the low mass stars in six open clusters spanning from ZAMS to solar age. Table 1 provides an overview over the final sample. The literature overview of age, distance, and metallicity determinations is given in Table **??** in the Appendix. Membership probability histograms of the final sample are displayed in Figure **??**.

2.3.1. Pleiades

The Pleiades, a nearby ZAMS cluster, were observed in Campaign 4, and were treated in PaperI. We include the cluster in this work for completeness and to illustrate improvements to (PaperI). We revisited the memberships from Rebull et al. (2016a), which were your in the previous work, and merged them with lists of members determined by Olivares et al. (2018); Gaia Collaboration et al. (2018a); and Cantat-Gaudin et al. (2018).

2.3.2. M35

M35 is a ZAMS cluster 900 pc away, observed during Campaign 0 in K2. We merged membership lists from Cantat-Gaudin et al. (2018); Gaia Collaboration et al. (2018a); and Bouy et al. (2015). There are only five K2 light curves, but we identified multiple additional members with publicly available[1] light curves obtained from Soares-Furtado et al. (2017). They used an image subtraction technique in the campaign's super stamps, a self flat-fielding de-trending inspired by K2SFF (Vanderburg & Johnson 2014), and a trend-filtering algorithm developed by Kovács et al. (2005). We preferred PSF photometry in cases where both aperture K2 and PSF LCs were available. We took the raw extracted PSF light curves and de-trended them using K2SC.

2.3.3. Hyades

The Hyades are a 0.6 Gyr old OC observed during Campaigns 4 and 13 with K2. It is about as old as Praesepe. We merged membership tables obtained from Douglas et al. (2014); Reino et al. (2018); and Gaia Collaboration et al. (2018a).

---

[1] https://k2.hatsurveys.org/archive/

Table 1. Open clusters.

	d [pc]	stars	LCs	flares	campaigns	age [Myr]	[Fe/H]
Pleiades	135.6	761	761	1606	1	$135\binom{25}{25}$	$-0.04(0.03)$
Hyades	46.0	171	171	396	2	$690\binom{100}{160}$	$0.13(0.02)$
Praesepe	185.5	964	964	906	3	$750\binom{7}{3}$	$0.16(0.00)$
Rup 147	305.0	53	53	9	1	$2650\binom{380}{380}$	$0.08(0.07)$
M67	908.0	307	307	1	3	$3639\binom{17}{17}$	$-0.10(0.08)$

Notes. n is the approximate number of members with $p > 0.8$. LCs, SLCs, LLCs, and PSF LCs denote the number of available light curves, short cadence light curves, long cadence light curves, and PSF de-detrended light curves, respectively. The values for age, [Fe/H], and distance are approximate values from a comparison of existing literature, detailed in Appendix B.1.

2.3.4. Praesepe

Praesepe appeared in Campaign 5, and was previously treated in PaperI. It was then observed again during Campaign 13. We revisited the memberships obtained by Douglas et al. (2014), and matched them to the members identified in Douglas et al. (2017); Rebull et al. (2017); Cantat-Gaudin et al. (2018); and Gaia Collaboration et al. (2018a).

2.3.5. Ruprecht 147

Ruprecht 147 is a 2.5 Gyr old OC observed during Campaign 7 with K2. We used the mean membership probabilities obtained from a number of studies (Curtis et al. 2013; Cantat-Gaudin et al. 2018; Olivares et al. 2019) combined with the members found by Gaia Collaboration et al. (2018a) to identify the most likely members.

2.3.6. M67

M67 is a solar-age, solar metallicity OC about 900 pc away. Multiple members were observed during Campaign 5, and revisited in Campaigns 16 and 18. We did not find any flares in M67 in Campaign 5 (PaperI) observing the members identified by Gonzalez (2016). The recent campaigns brought both additional observations, and entirely new targets to the sample. We merged the members from Gonzalez (2016) with a recent study based of Gaia DR2 data (Gao 2018). Additionally, we obtained PSF-detrended light curves for Campaign 5 from Nardiello et al. (2016).

2.4. Effective temperatures, stellar radii, and luminosities

2.4.1. Photometry and extinction correction

We determined effective temperatures T_{eff} using broadband photometry the Two Micron All Sky Survey (2MASS; Skrutskie et al. 2006), the Panoramic Survey Telescope and Rapid Response System (Pan-STARRS) Data Release 1 (Chambers et al. 2016), and Gaia DR2 (Gaia Collaboration et al. 2018b). We applied quality cuts to 2MASS, Pan-STARRS DR1, and GaiaDR2 data, as described in Appendix C, and removed foreground stars using Gaia DR2 parallaxes. We corrected the 2MASS and PanSTARRS photometry in M35, M67, and Ruprecht 147 for extinction using the most recent version (Green et al. 2019) of the `dustmaps` package that provides 3D dust maps derived from 2MASS and PanSTARRS photometry together with Gaia distances (Green et al. 2018). If there was no Gaia parallax available we used the cluster median distance instead.

If an extinction value was not available for a given star we used the average extinction value of the respective cluster. We accounted for extinction in Gaia BP and RP using the reddening $E(B_P - R_P)$ derived from Gaia photometry and parallax from Gaia DR2 (Andrae et al. 2018). We dropped targets that were too bright (Kepler magnitude $K_p \leq 9$).

2.4.2. Effective temperatures

We applied several methods and color-temperature relations (CTRs) to determine robust T_{eff}. We used CTRs from Boyajian et al. (2013) and Mann et al. (2016) (erratum to Mann et al. 2015), and T_{eff} derived from Gaia DR2 using the StarHorse algorithm (Queiroz et al. 2018) and inferred from Gaia DR2 using the Apsis pipeline (Bailer-Jones et al. 2013; Andrae et al. 2018). Boyajian et al. (2013) determined CTRs from a range of interferometrically characterized stars using $g - z$, $g - i$, $g - r$, $g - J$, $g - H$, and $g - K$ colors from SDSS and Johnson magnitudes for A to K stars. Their sample is centered on solar metallicity, so we constained the use of these CTRs to stars with $-0.25 < [\text{Fe/H}] < 0.25$. We transformed 2MASS JHK to $J - H$, $H - K$, and $J - K$ in the Johnson system as the authors from 2MASS to the Bessell-Brett sytem (Carpenter 2001), and from Bessell-Brett to Johnson using the relations in Bessell & Brett (1988).

Mann et al. (2015) provide CTRs from absolutely calibrated spectra to which they fitted atmospheric models to obtain T_{eff}. Alternatively, they determined T_{eff} from long-baseline optical interferometry measurements using the bolometric flux. Among others, they note transformations for SDSS/2MASS $r - z$ and $r - J$, or Gaia $BP - RP$ where extra information can be added from metallicity or 2MASS $J - H$. The relations in Mann et al. (2015) are only valid if metallicity is sufficiently close to solar, which is satisfied for all clusters in this paper (see Table **??**). M35 may be an exception to this rule.

We supplemented our estimates with T_{eff} estimates from Anders et al. (2019) who used the StarHorse pipeline (Queiroz et al. 2018) on Gaia DR2.

Gaia DR2 published effective temperatures for over 160 million sources (Gaia Collaboration et al. 2018b). The typical uncertainty is quoted at 324 K, but it is lower for stars above ∼4100 K and below ∼6700K, so that we adopt 175 K which is above the quoted root-median-squared error in this T_{eff} range (Andrae et al. 2018), and use provided values only in this range.

Empirical CTRs suffer from systematic errors that stem both from the different methods applied, and from sample selection biases. We used as many empirical relations as possible in their appropriate ranges to obtain multiple T_{eff} estimates from which
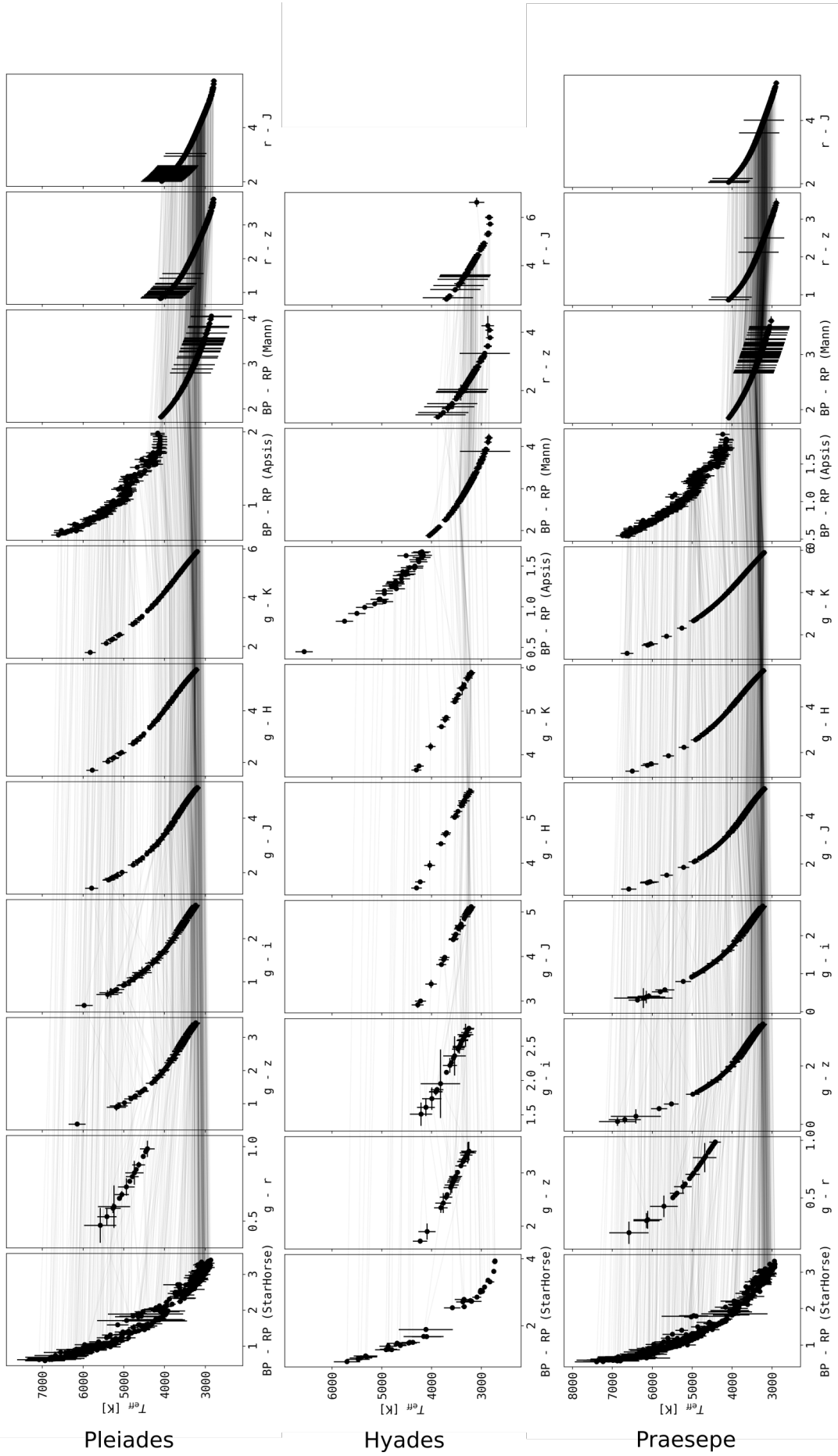
Fig. 2. Color-temperature relations for Pleiades, M35, and Hyades.
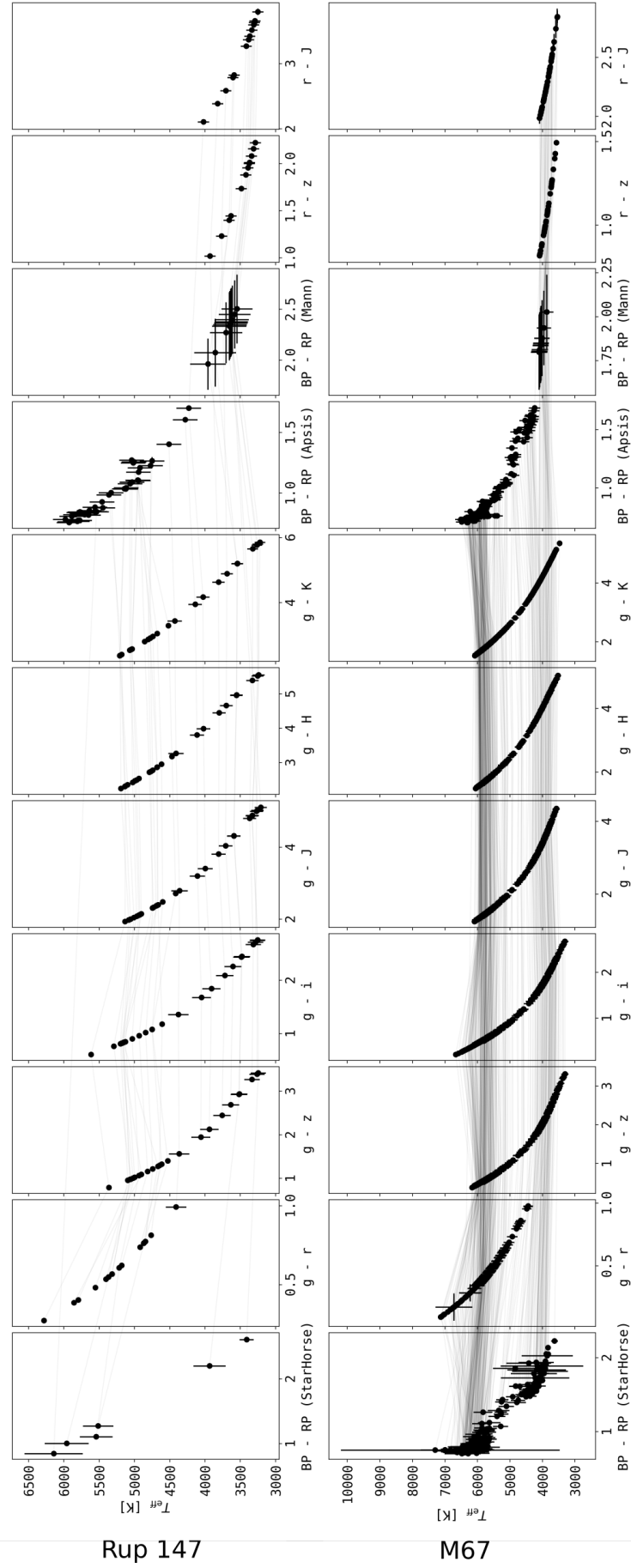
Fig. 3. Color-temperature relations for Praesepe, Ruprecht 147, and M67. Description as in Fig. 2.
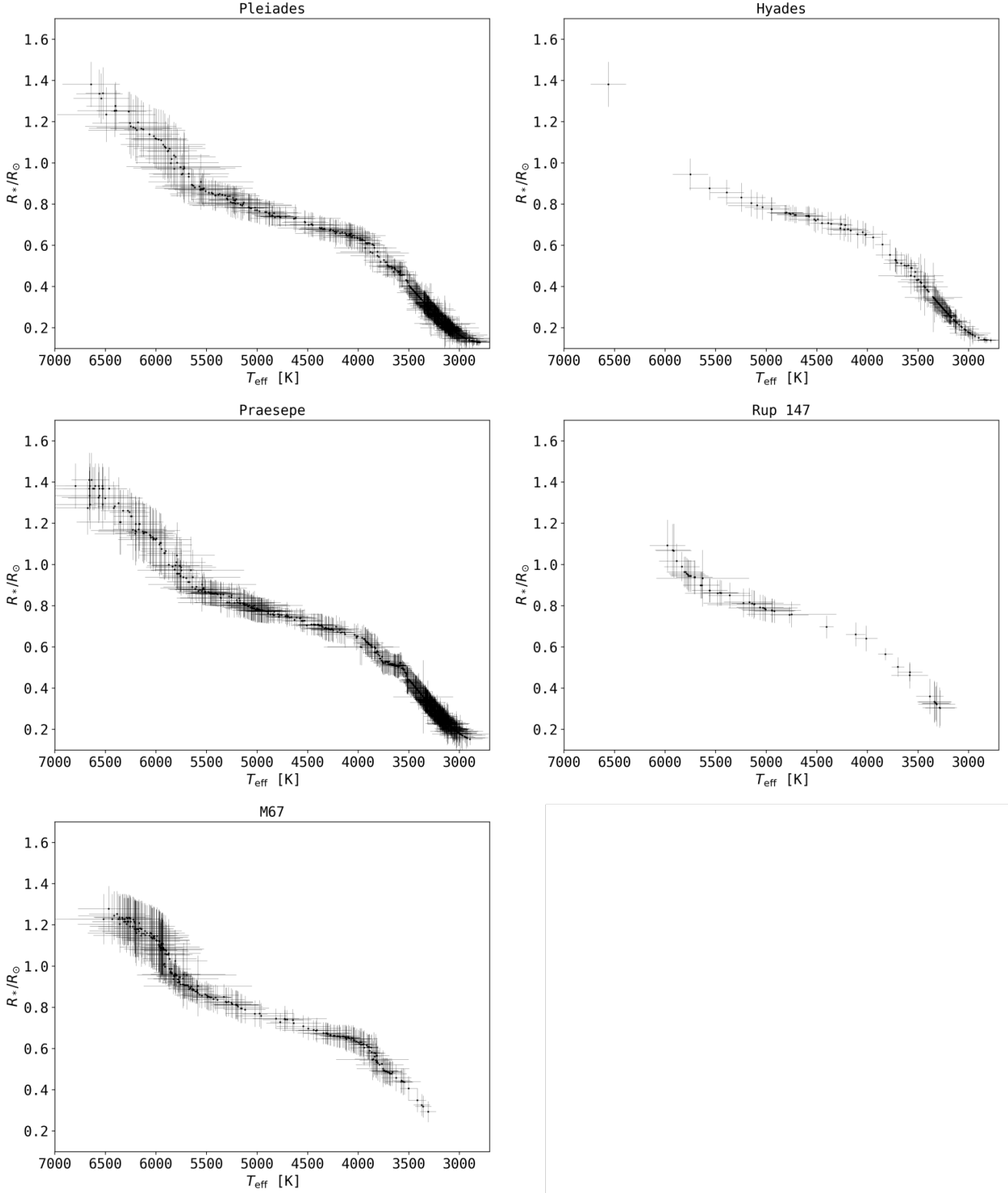
Fig. 4. $T_{\rm eff} - R_*$ relation for all clusters in this study.

we then drew a more reliable median value. Targets that were lacking sufficient photometric data to derive $T_{\rm eff}$, or were too hot to be expected to have a convective envelope ($T_{\rm eff} \geq 7000$;K), were flagged accordingly, and removed from the sample. We dropped all targets where the uncertainty on the weighted mean

$T_{\rm eff}$ was greater than 10%. Only targets that were assigned a $T_{\rm eff}$ were searched for flares.

2.4.3. Stellar radii

We used a catalog of empirically characterised stars (Yee et al. 2017) to derive R_* from T_{eff} (Fig. 4). Yee et al. (2017) collected 404 stars with high-resolution spectra from the literature, and own observations of mid to late K-dwarfs, spanning low mass stars from 7000 K down to 3000 K. For these stars, the resulting catalog is accurate to 100 K in T_{eff}, 15 % in R_*, and 0.09 dex in [Fe/H]. We interpolated between stars from the catalog to our derived T_{eff}, and propagated the resulting scatter to the uncertainty in R_* if $T_{eff} > 3500$ K. For stars with $T_{eff} < 3500$ K we used $T_{eff} - R_*$ relations derived by (Mann et al. 2015, 2016).

2.4.4. Spectra

We assigned spectra to our targets from the SpecMatchEmp Yee et al. (2017) and the FlareSpecPhot libraries (Schmidt 2014; Kirkpatrick et al. 2010; Burgasser et al. 2007, 2008, 2010, 2004; Cruz et al. 2004; Burgasser & McElwain 2006; Rayner et al. 2009; Doi et al. 2010; Filippazzo et al. 2015; Cruz et al. 2003; West et al. 2011; Bochanski et al. 2010, 2007; Schmidt et al. 2010, 2015, 2014; Mann et al. 2015). When a specturm was available for the derived spectral type in FlareSpecPhot, we preferred it over SpecMatchEmp, which was the case for all stars cooler than M0, where we mapped spectral type to effective temperature as appears in Pecaut & Mamajek (2013). We then combined stellar radii R_*, T_{eff}, and spectra to projected bolometric luminosities $L_{bol,*}$, and projected luminosities in the Kepler band $L_{Kp,*}$ (Shibayama et al. 2013; Ilin et al. 2019). Uncertainties on $L_{Kp,*}$ ranged from 9 % to 52 % with a median value of 17 %.

3. Methods

We detected flare candidates automatically, and validated them by eye. We attempted to assign recovery probabilities and corrected for sampling effects using injection/recovery tests but the procedure was not scalable due to computational costs. We performed injection recovery on a handful of example light curves to see that de-trending and intrinsic light curve properties smear out the ED recovery with varying distributions that add an uncertainty of about 30%. Most of the candidates are expected to have a complex shape that deviates from the classical flare template. The validation yielded an estimate on the uncertainty on the flare energy released in the Kepler band. The frequency distributions of these flare energies are believed to follow a power law that spans multiple orders of magnitude. We adopted this model, and used two different Maximum Likelihood estimators to obtain the power law exponents. We tested the best fit parameters with the Kolmogorov-Smirnov test, and probed possible truncation of the power law relation with an exceedance test.

3.1. Flare finding

We used the open source software `AltaiPony`[2] to automatically detect and characterize flares in our sample. The code base relies on K2SC[3] (Aigrain et al. 2016) to remove instrumental and astrophysical variablity from K2 light curves. We did not use the de-trended light curves available on MAST[4], but used K2SC to de-trend light curves from the re-processed final data release. We clipped outliers at 3σ iteratively, as compared to the original

---

[2] `altaipony.readthedocs.io`
[3] `github.com/OxES/k2sc`
[4] `archive.stsci.edu/prepds/k2sc/`

work, where outliers were clipped at 5σ (Aigrain et al. 2016). After de-trending, the flare finder algorithm searched fo continuous observing periods, defined as being longer than 10 data points at a minimum cadence of 2 h. All further routines were run on these observing periods. The finder iteratively clipped excursions from the median value at 3σ rolling window noise above median plus uncertainty given from K2SC de-trending. After each iteration, outliers were cut down to the current median value. Either after convergence, or 50 iterations, the resulting median value was adopted. With this median as quiescent flux, flare candidates were identified with the same procedure as during the median value calculation, but now we additionally required at least three consecutive data points to fullfil the 3σ-criterion. Flare candidates were merged into single candidate events if they were less than four data points apart. For each of these candidates flaring time, amplitude and equivalent duration (ED) were returned.

ED is the area between the LC and the quiescent flux, that is, the integrated flare flux divided by the median quiescent flux F_0 of the star, integrated over the flare duration (Hunt-Walker et al. 2012):

$$ED = \int dt \, \frac{F_{flare}(t)}{F_0}. \tag{1}$$

ED is a quantity independent of calibration and distance that is suited to compare flaring activity on stars where these properties are uncertain. ED describes the time during which a star releases as much energy as the flare itself. This time can be shorter or longer than the actual flare duration.

The uncertainty in ED depends on the light curve noise properties, time sampling, and other intrinsic characteristics. Moreover, K2SC de-trending and the flare finding procedure introduce additional uncertainty that dominates the photometric noise. It was not feasible computationally to perform the injection and recovery of synthetic flare events to take into account the effects of GP regression that underlies K2SC. Instead we estimated the scatter in the residual flux using the iterative procedure that Schmidt et al. (2020) applied to TESS light curves.

The Kepler flare sample has shown to be difficult to treat in a fully automated way. Without manual vetting, the event samples remain significantly contaminated (Yang & Liu 2019). As K2 was subject to further technical difficulties, the expected contamination is rate was expected to be even higher. Some light curves could not be de-trended using K2SC alone. Light curves with extreme astrophysical signals like deep transits, rotational modulation on time scales of a few hours or passages of bright SSOs had to be masked accordingly or fitted with an additional sinusoidal component to the K2SC-treated time series. A number of light curves were excluded from the flare search because they saturated the detector, or because the target aperture overlapped with broken pixels. Some very faint targets and extreme variables could not be searched because the de-trending did not terminate successfully. The online version of Table 2 includes an additional flag and contains explanatory notes on the excluded targets.

3.2. Kepler flare energies

(see PaperI for details).

Multiband time resolved observations of active M dwarfs have shown that continuum flux accounts for the majority of the

energy radiated by flares (Kowalski et al. 2013). The effective temperature of this blackbody, however, varies by a great degree, with, to date, no robust predictor of that temperature:
While solar flares are relatively cool, with $T_{eff} \approx 5\,000 - 7\,000$ K (Kleint et al. 2016; Kerr & Fletcher 2014; Watanabe et al. 2013; Namekata et al. 2017), SEDs of stellar flares tend to be blue (**?**). At least one M dwarf flare reached $40\,000$ K as seen in FUV spectra (Froning et al. 2019), and most events exhibit temperatures of about $9\,000 - 10\,000$ K (Hawley & Fisher 1992; Kretzschmar 2011; Shibayama et al. 2013). A dependence of flare temperature on stellar age, or mass, or both, will enter our analysis if we attempt to quantify bolometric flare energy. At about $6\,200$ K, the Kepler pass band captures the largest flux fraction, at $10\,000$ K $72\,\%$, at $40\,000$ K only $4\,\%$ of this value is transmitted. Another effect is that flares of equal flare energy but hotter SED would not be seen in the Kepler band at all.
We propagated the uncertainties σ_{ED} and σ_L (on $L_{*,Kp}$) in quadrature to $E_{Kp,flare}$.

3.3. Power law fits

The power law exponent determined for flare frequency distributions has consistently been found to be independent of spectral and age (Davenport et al. 2019) for solar-type and low mass dwarfs (see Table F.1 in the Appendix).
Flare frequency distributions follow power law relations that cover several orders of magnitude, from solar microflares to stellar superflares. We fitted power law functions to the FFDs in ED and E_{Kp} space using a stabilized maximum likelihood estimator (MLE) (Maschberger & Kroupa 2009). As recommended by Maschberger & Kroupa (2009), we applied the stabilized Kolmogorov-Smirnov (KS) test at $95\,\%$ significance level to all power law fits in the sample. If the test fails the power law model does not fit the data at the given significance level. If the test passes, this does not give any information whether the power law model is the correct assumption. The goodness of fit can be estimated from the visual inspection of percentile-percentile plots, given in the online material[5]. It is not straighforward to account for the deviation from an ideal power law at low energies, because the aforementioned effects may be partly cancelled by background contamination from, for instace, cosmic rays (**?**). We believe that we are mostly limited by the non-linear dependence for the energy bias from time sampling effects (**?**) and recovery probability on flare duration and amplitude. These parameters are not resolved in FFDs, and while they are correlated there is significant spread in the duration-amplitude relation to blur the cutoff in th e FFD. One way to account for this circumstance is to inject and recover synthetic flares with a variety of durations and amplitudes and to determine energy ratios and recovery probabilities for each individual candidate, assuming that the underlying flare shape can be sufficiently well parametrized, as was first explored in Davenport et al. (2014) for Kepler data and expanded in (Schmidt et al. 2020) for TESS.
The second method used the MLE result as a prior for α. Following Wheatland (2004), we defined the joint posterior distribution for the probability ϵ that a flare with ED or energy above some

value S_2 occurs within a time period ΔT:

$$
\begin{aligned}
p(\epsilon, \alpha) = \; & C \cdot (-\ln(1-\epsilon)^M) \\
& \cdot (\alpha - 1)^M \cdot \Gamma(\alpha) \left[\frac{(S_2/S_1)^{M+1}}{\pi} \right]^\alpha \\
& \cdot (1-\epsilon)^{(T/\Delta T) \cdot (S_2/S_1)^{\alpha-1} - 1}.
\end{aligned} \tag{2}
$$

C is the normalisation constant, M is the number of events, T the total observation time. Γ contains the prior distribution for α, and S_1 denotes the detection threshold above which all flares are detected. π encapsulates the flare energies as

$$
\pi = \prod_{i=1}^{M} \frac{s_i}{S_1} \tag{3}
$$

, where $\{s_1, s_2, ...s_m\}$ are the flare energies or ED.
The posterior distribution in Wheatland (2004) captures both the Poissonian distribution of flare events in time, and their power law distribution in energy, simultanesously. Wheatland (2004) derived this model to be able to predict the flaring rate of a given active region on the sun, and offered an extension to Eq. 2 that treated changing flaring activity rates as the active region evolves, and also characteristics of the active region itself, such as sunspot classifiers. In our simplification of the model, we assumed that the flare generating process did not change within the observation time span in any star in our sample ($M = M'$ in Eq. 24 in Wheatland (2004)). Another assumption was that this process was the same for all stars in the sample ($\Lambda_{MC} = 1$ in Eq. 24). Under these assuptions the information gained from the light curves could be stacked together.
With a uniform prior for α the results from the MLE and Markov Chain Monte Carlo (MCMC) sampling from the posterior distribution are the same, the latter allowed us to fit for ϵ and α simultaneously. Another advantage of the latter approach is that we could use more informative priors.
We chose our prior to reflect the power law exponent results discussed in the literature. The studies we took into account analysed flare frequency distributions of stellar flares in the optical regime, and focused mostly on K and M dwarfs (Lurie et al. 2015; Howard et al. 2019a; **?**; **?**) or ultra-cool dwarfs (**?**) but also solar-type stars (Shibayama et al. 2013). We also used a Gaussian fit to α obtained from the posterior distribution using the full sample of flares as the prior for a subsequent Bayesian analysis of individual age and T_{eff} bins. Assuming that α is universal for all spectral types, ages, and flare energy ranges, we used this more informative, Gaussian prior to further constrain the flaring rates.
Additionally we calculated the exceedance statistic tr to test if the power law distribution was truncated. If tr is 1, the power law distribution is truncated at the high energy end. If tr is 0, no information was gained from the calculation. To derive tr, given a number n of observations X_n and a best fit value for the power law exponent, we generated 500 samples with n values from this best-fit distribution assuming no truncation, i.e. choosing an upper limit several orders of magnitude higher than X_{max}. We then proceeded to truncate the samples at thresholds T below the maximum observed value X_{max} and determined the average number N_{ex} of generated values that will exceed T. If the underlying power law is not truncated, N_{ex} declines with larger n, as larger X_{max} will be present in the original data. If the best fit power law exponent is steeper, N_{ex} will be underestimated. If the best fit power law exponent is flatter, N_{ex} will be overestimated. If the power law is not truncated, for $n >= 100$ N_{ex}/n will be $< 5\%$, for $20 < n < 100$, typically

$N_{ex}/n < 15\%$.

4. Results

Fig. **??** shows the $E_{\text{Kp,flare}}$ and ED detection thresholds, as defined by the recovery probability (see Sec. **??**). The thresholds in ED reflect the noise level in the light curves.

4.1. Flaring activity as a function of a age and T_{eff}

Flaring activity decays with age. Flaring fraction was observed to decline with galactic latitude for M dwarfs (Hilton et al. 2010)Howard+2019. Short rotation periods and high magnetic activity measured in Hα are strongly correlated (West et al. 2015). According to gyrochronology, fast rotation indicates young age (Barnes 2003), and slows down as the star ages. Here, we quantify how this decline unfolds for different spectral types. Except for the stars in our coolest temperature bin (M5.5-M8, 2 500-3 000 K), stellar flaring activity at a given age is always stronger for a cooler star. The exception is seen at cluster ages around 120 Myr.
What creates the strong emission in white light? Extended flare loops, maybe (**?**)

4.2. M67 and Rup 147

We found several flare candidates in stars that are members of M67 and Rup 147. However, all but the events that occurred on four stars were false postives (SSOs), or the stars were not single members. Flare candidates in these old clusters appeared on RS CVn binaries, cataclysmic binaries, Algol type binaries, spectroscopic and eclipsing bianries, and red giant stars. Excluding all these, we were left with one flare in M67 on a K1 dwarf. In Rup 147, we narrowed down the list to a flare on a G8 star in Rup 147, and four flares each on a K0.5 and an M3 star. For these stars, the multiplicity status is unknown. We found that the mass range of these stars as calculated from the uncertainties on their radii (**?**) is large enough that the stars could in principle be binary stars with undetected mid-M dwarf companions.

4.3. Flaring Activity Indicators

Flaring luminosity FA The energy released in flares was inferred using our derived stellar luminosities. It declines with age for every T_{eff} bin considered for both the total luminosity and relative to the quiescent flux (Fig. **??**).
$L_{\text{Kp,flare}}$ is the luminosity in flares in the Kepler band. We can relate this to the quiescent bolometric luminosity of the star when we define the fractional flare luminosity FA in analogy to PaperI:

$$FA = \frac{E_{\text{Kp,flare,tot,}}}{t \cdot L_{\text{bol,*,}}} \qquad (4)$$

We determined $L_{\text{bol,*}}$ from R_* and T_{eff}, as described in Sec. 2.4. In Fig. 8 we computed the median and standard deviation FA for every T_{eff} bin. FA is a meaningful measure of relative stellar activity as long as the flux portion of the quiescent star in the Kepler band is roughly constant. It is therefore more meaningful to compare FA values across age than across T_{eff}.

FFD   Power law fit parameters to the FFDs (Figs. **??** and **??**) are sensitive to the low-energy cutoff, where most observations reside. The goodness of fit strongly depends on the sample size. Power law fit parameters derived using MLEs, as described in Sec. 3.3, are mostly consistent with each other but often deviate from $\alpha = 2$. A smaller sample size tends to create a flatter distribution (Figs. 9 and **??**). Truncation was not detected for FFDs with more than 50 flares (Tables **??** and **??**) For these results, extrapolations outside of the observed energy range are clearly off. If we assume $\alpha \equiv 2$, different distributions can be compared. For fixed α, in the ED domain, β_2 is the flare frequency at $ED = 1$ s, and shows a trend in both T_{eff}, and age (see Fig. **??**). In the energy domain, the picture is less clear (Fig. **??**).
Compare to other FFD values, e.g., from Ward's Evryscope survey, see table in Appendix, and maybe convert it to a plot Howard et al (2019) monitored superflares on cool stars with bolometric energies above 10^{33} erg and up to 10^{36} erg. They find power law exponent values around ~ 2 resolved by spectral types. Similar values are found for individual flare stars (Lurie et al. 2015).
Howard+18, Loyd+18, Tilley+19 show that flares can erode exoplanetary atmospheres. If a flare is assumed to deposit its UV energy in an instant a single superflare can completely remove the ozone layer at the substellar point Loyd+18. Associated protons are safer way to ozone destruction if they are associated with reoccurring large flares Tilley+19

5. Discussion

5.1. Consistency with other studies

EvryFlare, mass-dependence,

5.2. Flaring and rotation

More energetic flares can be expected from faster rotating stars (Candelaresi et al. 2014; Doorsselaere et al. 2017; Yang et al. 2017). Findings that flares with intermediate Rossby number appear to flare more than fast and slow rotators (Mondrik et al. 2019) could not be reproduced here or in the EvryFlare survey (Howard et al. 2019b). If enhanced flaring can be interpreted as an increase in the stellar angular momentum loss rate flaring activity can be used to inform the cause of variation in the spin-down efficiency. An example of such variations is the apparent temporary stalling of spin-down seen in K dwarfs in NGC 6811 (Curtis+2019). The authors favored a scenario in which the stellar core transfers momentum onto the envelope but did not rule out the possibility of a decreased magnetic braking efficiency. In the latter scenario, these stars should flare less.
We used rotation periods derived from K2 light curves for the Pleiades (Rebull et al. 2016b), the Hyades (Douglas et al. 2016), and Praesepe (Rebull et al. 2017), to illuminate the rotation-flaring relation at fixed ages. In the Pleiades, most flaring stars are found on the fast rotator branch at or below one day, and flaring activity peaks in this regime. For Praesepe, flaring rates aappear t ..[...]. In the Hyades, all of the 11 stars with rotation periods that overlapped with our sample were found flaring, but the number were too low to provide statistical insight. For Rup 147 and M67, no rotation rates were available at the time.

5.3. M37

Comparing our results to a similar study of photometric flares in M37 (Chang et al. 2015) we find the results somewhat discrepant. M37 is 300-600 Myr old and appears less active than Praesepe and Hyades in individual Teff bins, which are of coeval

Table 2. Selection of confirmed flare candidates detected in open clusters observed by Kepler/K2, sorted by amplitude a. The full table is available on CDS.

| EPIC	C	cluster	c_0	c_1	a	T_{eff} [K]	ED [s]	$L_{bol,*}$ [erg/s]	L_{Kp} [erg/s]
211079830	4	Pleiades	105984	105993	15.330194	3097(87)	63340(63)	$8.29(3.34)10^{29}$	$3.32(1.34)10^{29}$
210720772	4	Pleiades	107181	107184	9.674757	3104(86)	19901(7)	$8.66(3.45)10^{29}$	$3.48(1.38)10^{29}$
247523445	13	Hyades	143106	143109	8.260956	2964(49)	16615(11)	$4.33(1.09)10^{29}$	$1.69(0.43)10^{29}$
212021131	5	Praesepe	108974	108980	7.421916	3215(68)	19828(175)	$2.01(0.65)10^{30}$	$8.22(2.65)10^{29}$
210978953	4	Pleiades	106762	106770	6.769888	3050(95)	39467(125)	$6.20(2.63)10^{29}$	$2.46(1.04)10^{29}$
211913613	16	Praesepe	156845	156849	6.690356	3218(66)	21632(147)	$2.05(0.65)10^{30}$	$8.37(2.63)10^{29}$
211127297	4	Pleiades	106754	106759	6.449569	3147(86)	20830(5)	$1.13(0.45)10^{30}$	$4.59(1.81)10^{29}$
211681193	5	Praesepe	108116	108120	5.570804	3182(76)	11198(95)	$1.64(0.58)10^{30}$	$6.68(2.37)10^{29}$
211024798	4	Pleiades	104822	104826	5.394897	3290(62)	12524(63)	$2.58(0.75)10^{30}$	$1.06(0.31)10^{30}$
211134185	4	Pleiades	103891	103896	4.951629	3127(96)	17459(33)	$9.99(4.33)10^{29}$	$4.03(1.75)10^{29}$
211095280	4	Pleiades	106283	106287	4.796979	3138(93)	12186(10)	$1.06(0.45)10^{30}$	$4.32(1.82)10^{29}$
211022535	4	Pleiades	104262	104267	3.994973	2953(76)	15164(57)	$3.50(1.10)10^{29}$	$1.37(0.43)10^{29}$
211010517	4	Pleiades	106680	106685	3.968907	3252(70)	16241(171)	$2.09(0.68)10^{30}$	$8.59(2.77)10^{29}$
210846442	4	Pleiades	104410	104415	3.959977	3311(79)	13515(10)	$2.88(0.96)10^{30}$	$1.18(0.40)10^{30}$
212017838	5	Praesepe	111183	111192	3.671037	3307(89)	10274(10)	$3.35(1.22)10^{30}$	$1.38(0.50)10^{30}$
211984058	5	Praesepe	109952	109965	3.320636	3124(97)	16063(149)	$1.17(0.51)10^{30}$	$4.73(2.06)10^{29}$
211912899	5	Praesepe	110700	110706	3.257997	3133(81)	7967(16)	$1.24(0.47)10^{30}$	$5.01(1.89)10^{29}$
211151674	4	Pleiades	106457	106467	3.166323	3072(93)	17843(106)	$7.10(2.99)10^{29}$	$2.84(1.19)10^{29}$
211822895	5	Praesepe	107809	107812	3.164494	3005(177)	6883(31)	$5.68(3.98)10^{29}$	$2.25(1.57)10^{29}$
211760567	5	Praesepe	109962	109965	3.061417	3245(58)	7838(9)	$2.39(0.69)10^{30}$	$9.84(2.83)10^{29}$
211939350	16	Praesepe	155018	155022	2.892939	3149(150)	9542(68)	$1.36(0.86)10^{30}$	$5.52(3.49)10^{29}$
211137806	4	Hyades	106768	106775	2.482828	3127(58)	9208(8)	$1.16(0.35)10^{30}$	$4.69(1.40)10^{29}$
210674207	13	Hyades	141708	141711	2.419586	3210(74)	5343(3)	$1.90(0.65)10^{30}$	$7.78(2.66)10^{29}$
211994910	5	Praesepe	109858	109864	2.401426	3325(95)	7807(14)	$3.71(1.40)10^{30}$	$1.53(0.58)10^{30}$
211010517	4	Pleiades	106561	106564	2.341076	3252(70)	4838(36)	$2.09(0.68)10^{30}$	$8.59(2.77)10^{29}$
211984058	5	Praesepe	108584	108587	2.155468	3124(97)	4817(13)	$1.17(0.51)10^{30}$	$4.73(2.06)10^{29}$
211983544	18	Praesepe	162792	162798	2.096077	3159(98)	6924(55)	$1.44(0.63)10^{30}$	$5.88(2.55)10^{29}$
210988354	4	Pleiades	106012	106017	2.057812	3661(144)	5725(1)	$1.40(0.31)10^{31}$	$6.06(1.32)10^{30}$
210886447	4	Pleiades	103871	103877	2.057490	3048(105)	8710(49)	$6.13(2.83)10^{29}$	$2.43(1.12)10^{29}$
211098921	4	Pleiades	105254	105262	2.041041	3300(101)	7499(5)	$2.72(1.10)10^{30}$	$1.12(0.45)10^{30}$
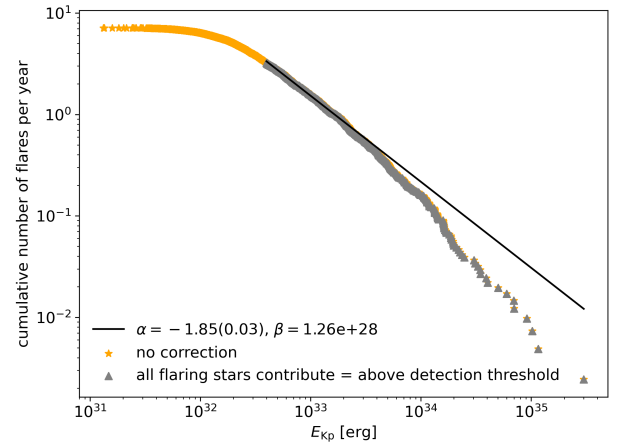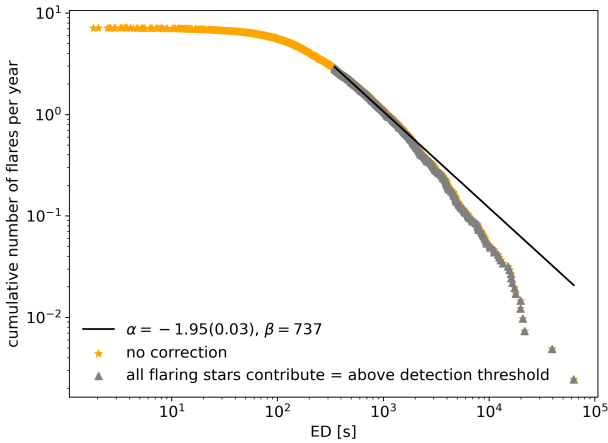
Fig. 5. FFD (scatter) in ED (left panel) and energy (right panel) and respective power law fit (black line) to the full sample of flare candidates.

Table 3. Mass budget of flaring stars in M67 and Rup 147 within uncertainties on radius.

| EPIC	median SpT	binary
211434440	K1	K2 + M5.5
219601739	G8	K1 + M6
219610232	K0.5	K2 + M5.5
219591752	M3	M3.5 + M3.5

or older. We attribute the difference to the loose membership requirement of $pmem \geq 0.2$ in Chang et al. (2015) as compared to our stricter cuts at 0.8. We expect the M37 to be contaminated with field stars that systematically reduce the flaring rates. Applying our own restriction the M37 sample (Chang et al. 2016) leaves very few flares that hamper a statistical description of their distributions.
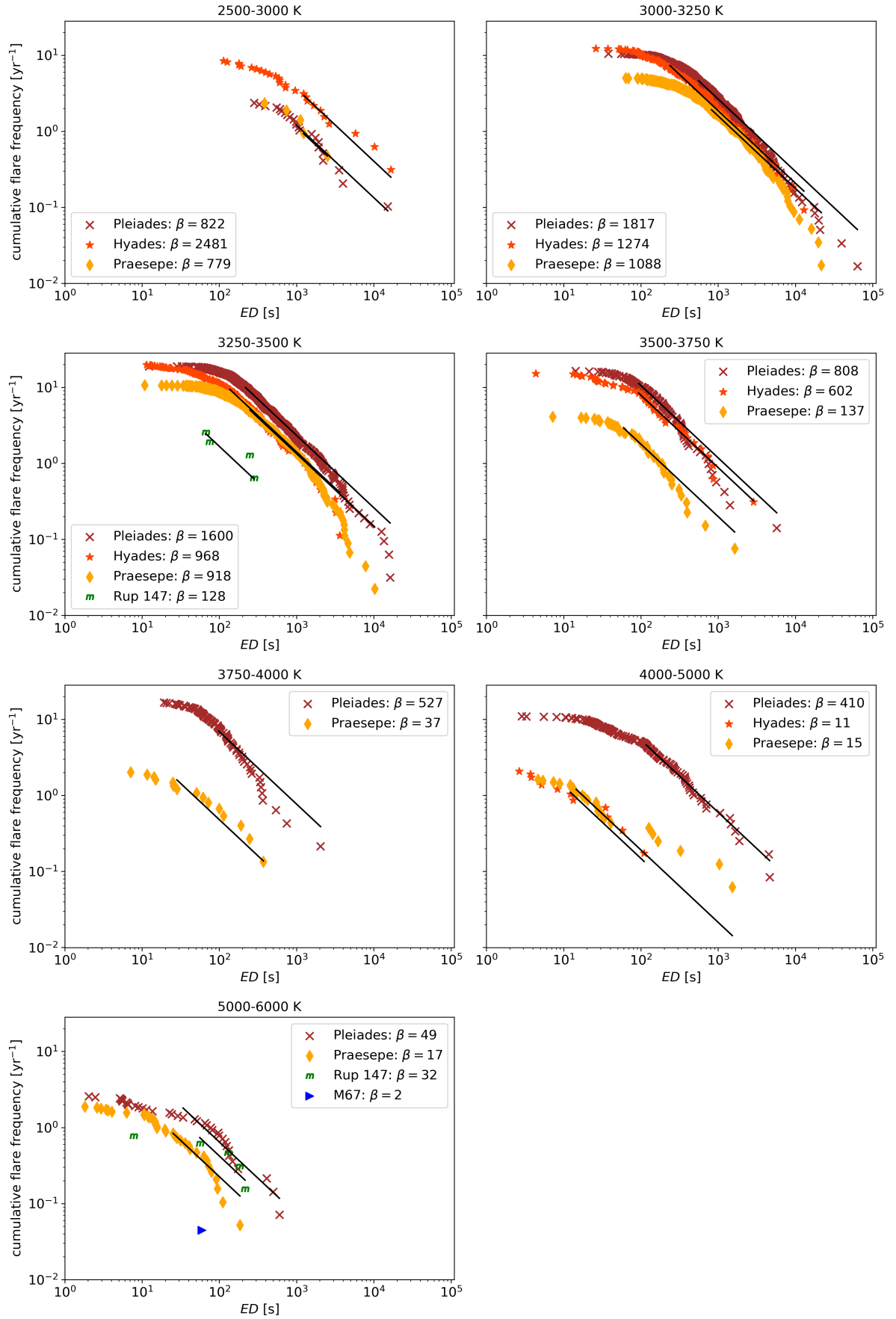
Fig. 6. FFDs (scatter) in *ED* and respective power law fits with $\alpha = XXX$ (black lines).
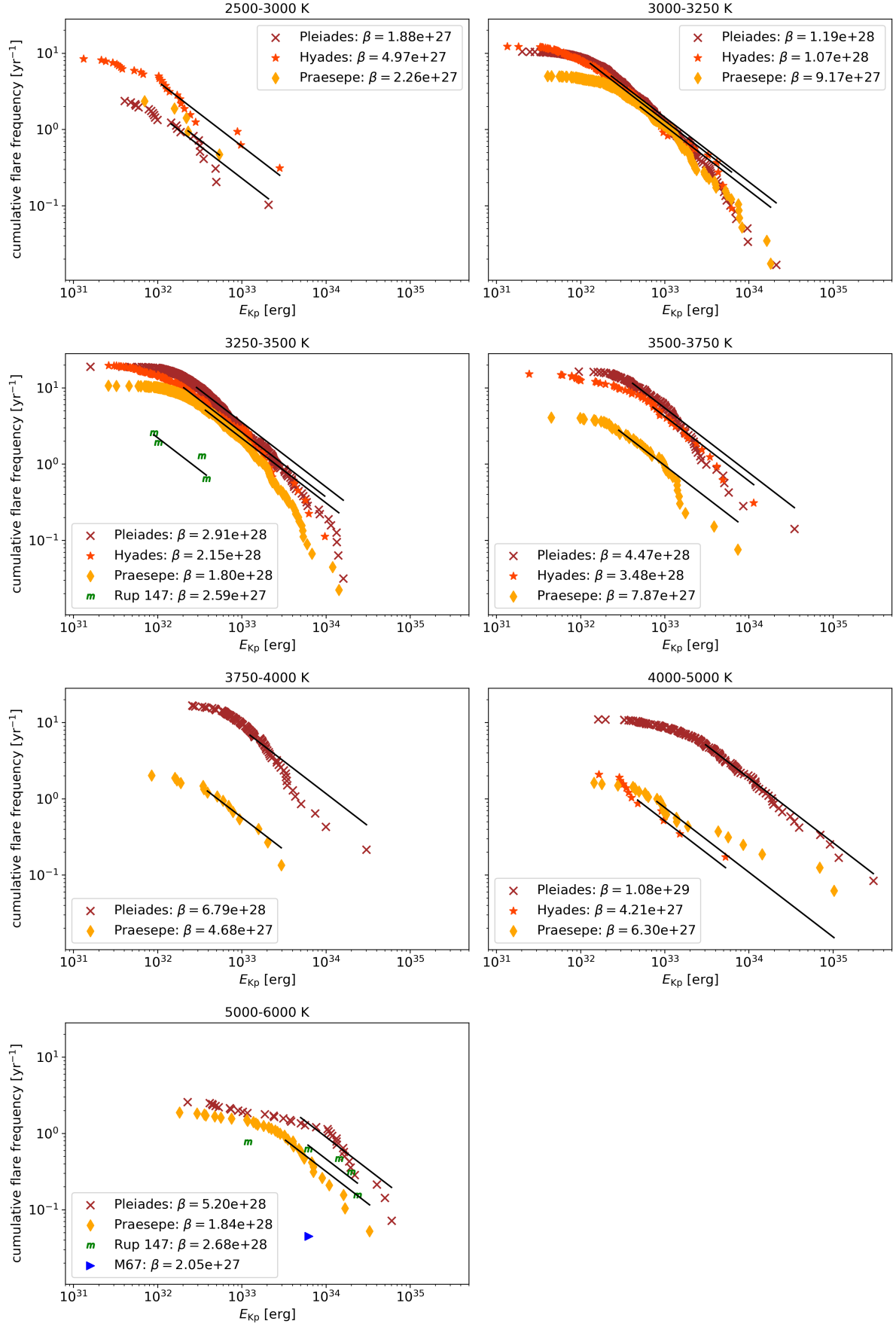
Fig. 7. FFDs (scatter) in energy and respective power law fits with $\alpha = XXX$ (black lines).
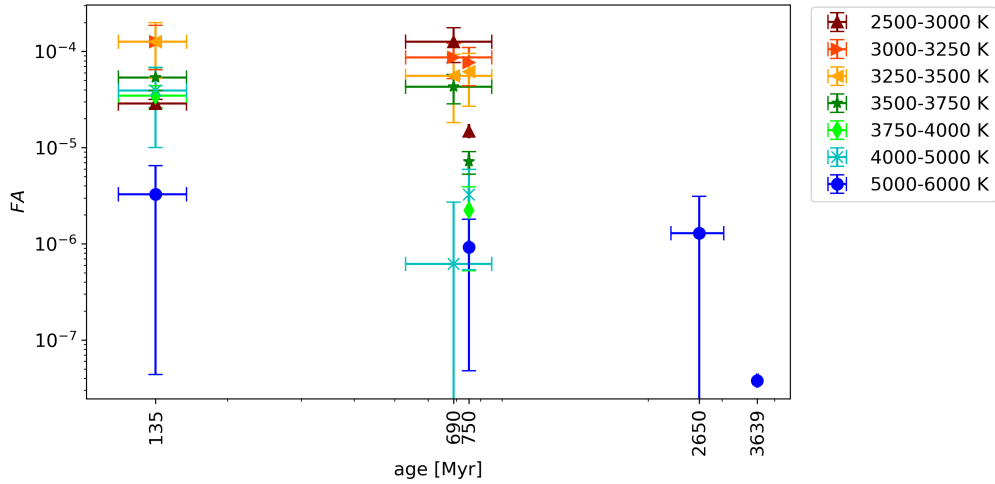
Fig. 8. *FA* for flares above the shared energy threshold as determined for the full FFD in Fig. 5.

Table 4. Summary of flaring β of all clusters and T_{eff} bins in E_{Kp} and ED distributions.

		β_s	n_s	tr_s	pl_s	β_{erg}	n_{erg}	tr_{erg}	pl_{erg}
2500-3000	Hyades	$2.48\,(0.1) \cdot 10^3$	27	False	True	$0.65\,(0.02) \cdot 10^{28}$	27	False	True
	Pleiades	$0.82\,(0.03) \cdot 10^3$	23	False	True	$2.46\,(0.09) \cdot 10^{27}$	23	False	True
	Praesepe	$0.777\,(0.024) \cdot 10^3$	5	False	True	$2.968\,(0.093) \cdot 10^{27}$	5	False	True
3000-3250	Hyades	$1.27\,(0.04) \cdot 10^3$	133	False	True	$1.401\,(0.038) \cdot 10^{28}$	133	False	True
	Pleiades	$1.814\,(0.055) \cdot 10^3$	623	False	True	$1.559\,(0.042) \cdot 10^{28}$	623	True	True
	Praesepe	$1.086\,(0.033) \cdot 10^3$	289	True	True	$1.205\,(0.033) \cdot 10^{28}$	289	True	True
3250-3500	Hyades	$0.966\,(0.03) \cdot 10^3$	175	False	True	$2.812\,(0.076) \cdot 10^{28}$	175	False	True
	Pleiades	$1.597\,(0.049) \cdot 10^3$	598	True	True	$0.382\,(0.01) \cdot 10^{29}$	598	True	True
	Praesepe	$0.917\,(0.028) \cdot 10^3$	477	True	True	$2.36\,(0.064) \cdot 10^{28}$	477	True	False
	Rup 147	$1.28\,(0.12) \cdot 10^2$	4	False	True	$0.34\,(0.03) \cdot 10^{28}$	4	False	True
3500-3750	Hyades	$0.6\,(0.02) \cdot 10^3$	49	False	True	$0.458\,(0.014) \cdot 10^{29}$	49	False	True
	Pleiades	$0.807\,(0.025) \cdot 10^3$	116	False	True	$0.588\,(0.016) \cdot 10^{29}$	116	False	True
	Praesepe	$1.36\,(0.05) \cdot 10^2$	54	False	True	$1.032\,(0.031) \cdot 10^{28}$	54	False	True
3750-4000	Pleiades	$0.53\,(0.02) \cdot 10^3$	78	False	True	$0.89\,(0.03) \cdot 10^{29}$	78	False	False
	Praesepe	$0.37\,(0.08) \cdot 10^2$	15	False	True	$0.61\,(0.02) \cdot 10^{28}$	15	False	True
4000-5000	Hyades	$1.13\,(0.11) \cdot 10^1$	12	False	True	$0.55\,(0.06) \cdot 10^{28}$	12	False	True
	Pleiades	$0.41\,(0.013) \cdot 10^3$	131	False	True	$1.434\,(0.039) \cdot 10^{29}$	131	False	True
	Praesepe	$1.46\,(0.07) \cdot 10^1$	26	False	True	$0.83\,(0.03) \cdot 10^{28}$	26	False	True
5000-6000	M67	$2.19\,(0.31) \cdot 10^0$	1	True	False	$2.70328\,(0.00027) \cdot 10^{27}$	1	True	False
	Pleiades	$0.49\,(0.05) \cdot 10^2$	36	False	True	$0.69\,(0.04) \cdot 10^{29}$	36	False	True
	Praesepe	$1.73\,(0.06) \cdot 10^1$	36	False	True	$2.44\,(0.09) \cdot 10^{28}$	36	False	True
	Rup 147	$0.32\,(0.08) \cdot 10^2$	5	False	True	$0.36\,(0.05) \cdot 10^{29}$	5	False	True

Table 5. Summary of FFD parameters and power law fits to the full sample of all clusters in E_{Kp} and ED space.

	ED	E_{Kp}
α	1.95(0.03)	1.85(0.03)
β [yr^{-1}]	785(24)	$1.75(0.05)10^{28}$
n_{tot}	2913	2913
n_{fit}	1166	1336
tr	True	True
pl	False	False

5.4. Division at 3000 K

The lowest T_{eff} bin at Pleiades age in our sample reflects the division between fully convective stars and those with a radiative core (Reid & Hawley 2005). At this age, the coolest dwarfs may still be accreting angular momentum on the PMS, instead of spinning down on the MS. We suggest that a regime change occurs around 120 Myr for stars with $T_{\text{eff}} = 2500 - 3250$ K.

Below 3000 K, an analysis of 66 ZDI maps show that magnetic field configurations can be strong and dipolar or weak and multipolar (Morin et al. 2008; See et al. 2017). If these stars can be distinguished by age, this should be reflected in our age-resolved flaring activity. If the difference is not a function of age, we should see a similar bimodal distribution of very inactive and very active stars in the lowest mass bins. If the difference between the two configurations is a function of age, we should only see one type of stars with correspondingly similar behaviour in these T_{eff} bins.

The lowest mass bin appears underactive compared to the rest of the flaring-age-T_{eff} relation in the ED domain. Physical explanations for this peculiarity include: A different magnetic structure
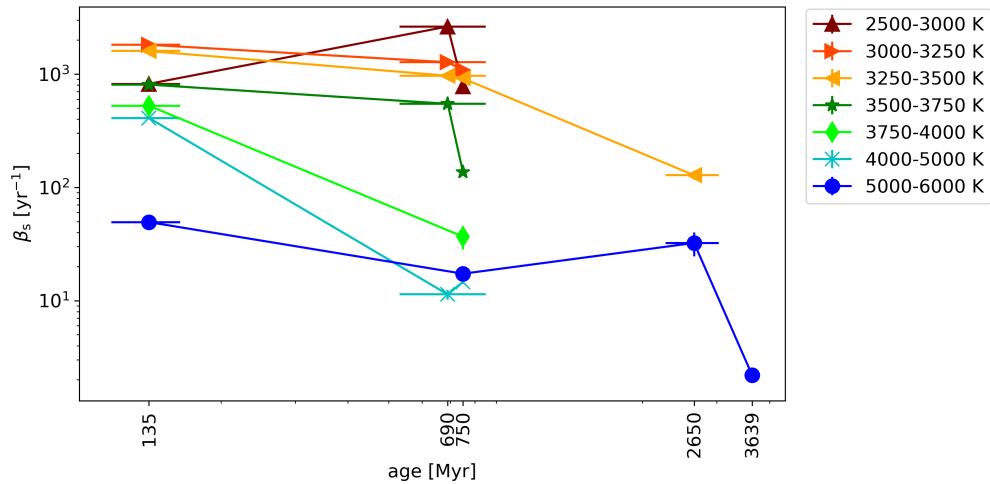
Fig. 9. Flare β_s vs. age grouped by T_{eff}.

A truncation of the power law that reflects the maximum *ED* an active region can produce on these stars.

West et al. (2015) found that all M1-M4 dwarfs with rotation periods shorter than 26 days, and all M5-M8 dwarfs with periods shorter than 86 days show Hα emission, indicating their magnetic activity.

Assuming a typical binary fraction for early and mid M dwarfs (Fischer & Marcy 1992), we can expect some of the flares on stars at $T_{\mathrm{eff}} > 3000$ K to belong to unresolved binary companions with $T_{\mathrm{eff}} < 3000$ K. A misattributed flare on an early M dwarf then will be assigned a too small *ED*, but still a correct $E_{\mathrm{Kp,flare}}$ because the count ratios are equal to the L_{Kp} ratios.

5.5. Consistency of Hyades' and Praesepe's results

HRDs constructed in Gaia Collaboration et al. (2018a) indicate only slightly older ages for Hyades and Praesepe. We expect our results to reflect this similarity.

Are the samples comparable? Membership determination may differ. Can we frame this as a statistical test, i.e. answer the question: What is the probability that the activity distributions for both clusters were drawn from the same underlying distribution for a given age and mass bin?
Metallicity is controlled for ([Fe/H](Praesepe) = 0.16, [Fe/H](Hyades) = 0.13, Netopil et al. 2016).

5.6. Jim's section(s)

Flaring activity function of mass and age − a gyrochronology analog?
Results in the context of Davenport et al. (2019): How well does the model fit if we have isochronal and not rotational ages for our stars?
Davenport et al. (2019) note a sample bias towards more active stars. Their models overpredicts the superflaring rate of the average Sun-like sample from Shibayama et al. (2013) and more resembles the rate for their most active sub-sample. *Do we see the same effect in our OC sample? We should not. Or cluster memberships depend on activity.*

The frequency of superflares at 10^{34} erg in the most active G-dwarfs and Sun-like stars in Kepler was once in 10–100 days, and every 800 years on average Sun-like stars. Benchmarking on the flare detected on a K1 dwarf in M67 in the G to early K bin

(5000-6000 K), and accounting for the fraction of the total flare energy that the Kepler passband covers at a flare temperature of 10 000 K, we found the flaring rate at this energy to amount to about once every 10 years. Doing the same for the Pleiades stars yielded that ZAMS G to K dwarfs flare once in 140 days at 10^{34} erg.

5.7. Universality of α

Taking into account uncertainties and systematic errors resulting power law fitting methods, the power law exponent $\alpha \sim 2$ appears to be the same for all studies on flare statistics so far, irrespective of spectral type. A notable exception are A stars in Kepler that follow a power law with $\alpha \sim 1$ that may indicate a different physical process (Yang & Liu 2019).
The values derived for α in our sample were both < 2. We argue that this was an effect of low recovery probability and energy fraction recovery for the smallest flares that were used to fit ther power law, as both effects are present and can be quantified using injection-recovery of synthetic flares (Schmidt et al. 2020 in prep.) that was not possible for our sample.

5.8. Deviations from single power law

Full sample is not consistent with a power law while the subsamples for different effective temperatures and ages mostly are. This can be interpreted as ..
Spots can survive on the stellar surface from a few days to nearly a year (Namekata et al. 2017; Davenport 2015). Namekata et al. (2017) find conceivable that spots evolve on timescale shorter than the estimated lifetimes. Complex spot geometry is correlated with the stongest X-class flares on the Sun (Toriumi et al. 2017; Sammis et al. 2000). This support the idea that flares are associated with the presence of certain types of starspots, or more generally, certain types of active regions. Since we can reasonable expect that there is a maximum flare energy a spot can produce, the underlying power law relation must break a some ED_{max}. We tested a possible truncation of our FFDs, but find no conclusive evidence for it in any FFD with > 50 data points. As we stack multiple targets, each potentially with multiple, evolving spots of various sizes on their surfaces, into one FFD at a time, we might observe a deviation but no truncation. A different explanation is simply that we do not sample the maximum

energies, as extremely high relative fluxes have been observed in the past (Paudel et al. 2018; Jackman et al. 2019; Schmidt et al. 2016).

6. Summary and Conclusions

Is there or will be there more data available to further extend the sample? There are no model-independent stellar ages. It is more correct to speak of evolutionary stage. Stars in open clusters with precise isochronal ages have their observables reduced to a number of years. We can now ask: Can we unambiguously map flaring evolutionary stage to the evolutionary stage of isochronal fit parameters of a given star? If there is either a strong correlation, or even a physical relation between flaring activity and, for instance, mass and rotation rate, the answer is yes. If this relation is sufficiently sensitive to be captured by present day instrumentation, and non-degenerate in the relevant parameters, flaring activity can be integrated into the family of age indicators, and complement and extend them.

Ultimately, flaring activity depends on how efficiently the star converts its energy budget to flares throughout its lifetime. Since the fraction of total luminosity released in flares is small even for the most active stars, this efficiency need not scale directly with the overall energy budget of the star on the MS, but will more likely depend on the ability of the star to use this budget to produce magnetic surface topologies and strengths that enable flaring.

A magnetic dynamo, driven by rotation and convection, introduces magnetic field to the system that causes stellar wind that in turn removes angular momentum from the star, decreasing its rotation rate. Over time, the wind takes away more and more angular momentum, and the global magnetic field weakens. This is reflected in observations of chromospheric indicators (ZDI???). The decline is famously known as the Skumanich law, and gave rise to the rotational age-dating technique called gyrochronology. However, recent studies noted deviations from this rule, a stalling of the spin-down, and offered multiple competing explanations. It is not clear how these effects reflect on the small scale surface magnetic field. Chromospheric activity on solar type stars seems to continue to decline regardless of these rotational effects.

What about X-ray?

Observationally, not much can be directly said about the small scale topology of stellar magnetic fields beyond extrapolations from the solar case. On the Sun, chromospheric activity indicates line emission in excess of radiative equilibrium that is caused by magnetic fields. Likewise, magnetic field effects heat the corona

References

Aarnio, A. N., Matt, S. P., & Stassun, K. G. 2012, ApJ, 760, 9

Aarnio, A. N., Stassun, K. G., Hughes, W. J., & McGregor, S. L. 2011, Sol. Phys., 268, 195

Aigrain, S., Parviainen, H., & Pope, B. J. S. 2016, MNRAS, 459, 2408

Alvarado-Gómez, J. D., Drake, J. J., Cohen, O., Moschou, S. P., & Garraffo, C. 2018, ApJ, 862, 93

Anders, F., Khalatyan, A., Chiappini, C., et al. 2019, A&A, 628, A94

Andrae, R., Fouesneau, M., Creevey, O., et al. 2018, A&A, 616, A8

Bailer-Jones, C. A. L., Andrae, R., Arcay, B., et al. 2013, A&A, 559, A74

Barentsen, G., Hedges, C., Saunders, N., et al. 2018, arXiv e-prints, arXiv:1810.12554

Barnes, S. A. 2003, ApJ, 586, 464

Bauke, H. 2007, European Physical Journal B, 58, 167

Bessell, M. S. & Brett, J. M. 1988, Publications of the Astronomical Society of the Pacific, 100, 1134

Bochanski, J. J., Hawley, S. L., Covey, K. R., et al. 2010, AJ, 139, 2679

Bochanski, J. J., West, A. A., Hawley, S. L., & Covey, K. R. 2007, AJ, 133, 531

Bokeh Development Team. 2019, Bokeh: Python library for interactive visualization

Bouy, H., Bertin, E., Barrado, D., et al. 2015, Astronomy and Astrophysics, 575, A120

Boyajian, T. S., von Braun, K., van Belle, G., et al. 2013, The Astrophysical Journal, 771, 40

Burgasser, A. J., Cruz, K. L., Cushing, M., et al. 2010, ApJ, 710, 1142

Burgasser, A. J., Liu, M. C., Ireland, M. J., Cruz, K. L., & Dupuy, T. J. 2008, ApJ, 681, 579

Burgasser, A. J., Looper, D. L., Kirkpatrick, J. D., & Liu, M. C. 2007, ApJ, 658, 557

Burgasser, A. J. & McElwain, M. W. 2006, AJ, 131, 1007

Burgasser, A. J., McElwain, M. W., Kirkpatrick, J. D., et al. 2004, AJ, 127, 2856

Candelaresi, S., Hillier, A., Maehara, H., Brandenburg, A., & Shibata, K. 2014, ApJ, 792, 67

Cantat-Gaudin, T., Jordi, C., Vallenari, A., et al. 2018, A&A, 618, A93

Carpenter, J. M. 2001, The Astronomical Journal, 121, 2851

Chambers, K. C., Magnier, E. A., Metcalfe, N., et al. 2016, ArXiv e-prints [arXiv:1612.05560]

Chang, S.-W., Byun, Y.-I., & Hartman, J. D. 2015, ApJ, 814, 35

Chang, S. W., Byun, Y. I., & Hartman, J. D. 2016, VizieR Online Data Catalog, J/ApJ/814/35

Clarke, R. W., Davenport, J. R. A., Covey, K. R., & Baranec, C. 2018, ApJ, 853, 59

Cruz, K. L., Burgasser, A. J., Reid, I. N., & Liebert, J. 2004, ApJ, 604, L61

Cruz, K. L., Reid, I. N., Liebert, J., Kirkpatrick, J. D., & Lowrance, P. J. 2003, AJ, 126, 2421

Curtis, J. L., Wolfgang, A., Wright, J. T., Brewer, J. M., & Johnson, J. A. 2013, AJ, 145, 134

Davenport, J. 2015, PhD thesis, University of Washington

Davenport, J. R. A., Covey, K. R., Clarke, R. W., et al. 2019, ApJ, 871, 241

Davenport, J. R. A., Hawley, S. L., Hebb, L., et al. 2014, ApJ, 797, 122

Doi, M., Tanaka, M., Fukugita, M., et al. 2010, AJ, 139, 1628

Doorsselaere, T. V., Shariati, H., & Debosscher, J. 2017, ApJS, 232, 26

Douglas, S. T., Agüeros, M. A., Covey, K. R., et al. 2014, ApJ, 795, 161

Douglas, S. T., Agüeros, M. A., Covey, K. R., et al. 2016, ApJ, 822, 47

Douglas, S. T., Agüeros, M. A., Covey, K. R., & Kraus, A. 2017, ApJ, 842, 83

Drake, J. J., Cohen, O., Yashiro, S., & Gopalswamy, N. 2013, ApJ, 764, 170

Filippazzo, J. C., Rice, E. L., Faherty, J., et al. 2015, ApJ, 810, 158

Finkbeiner, D. P., Schlafly, E. F., Schlegel, D. J., et al. 2016, ApJ, 822, 66

Fischer, D. A. & Marcy, G. W. 1992, ApJ, 396, 178

Froning, C. S., Kowalski, A., France, K., et al. 2019, ApJ, 871, L26

Gaia Collaboration, Babusiaux, C., van Leeuwen, F., et al. 2018a, A&A, 616, A10

Gaia Collaboration, Brown, A. G. A., Vallenari, A., et al. 2018b, A&A, 616, A1

Gao, X. 2018, ApJ, 869, 9

Gao, X. 2018, The Astrophysical Journal, 869, 9

Gizis, J. E. 2013, ApJ, 779, 172

Gonzalez, G. 2016, MNRAS, 459, 1060

Green, G. M., Schlafly, E. F., Finkbeiner, D., et al. 2018, MNRAS, 478, 651

Green, G. M., Schlafly, E. F., Zucker, C., Speagle, J. S., & Finkbeiner, D. P. 2019, arXiv e-prints, arXiv:1905.02734

Hawley, S. L. & Fisher, G. H. 1992, ApJS, 78, 565

Hilton, E. J., West, A. A., Hawley, S. L., & Kowalski, A. F. 2010, AJ, 140, 1402

Howard, W. S., Corbett, H., Law, N. M., et al. 2019a, ApJ, 881, 9

Howard, W. S., Corbett, H., Law, N. M., et al. 2019b, arXiv e-prints, arXiv:1907.10735

Howell, S. B., Sobeck, C., Haas, M., et al. 2014, PASP, 126, 398

Hunt-Walker, N. M., Hilton, E. J., Kowalski, A. F., Hawley, S. L., & Matthews, J. M. 2012, PASP, 124, 545

Ilin, E., Schmidt, S. J., Davenport, J. R. A., & Strassmeier, K. G. 2019, A&A, 622, A133

Jackman, J. A. G., Wheatley, P. J., Bayliss, D., et al. 2019, arXiv e-prints, arXiv:1902.00900

Karoff, C. 2016, Nature Communications, 7, 11058

Kerr, G. S. & Fletcher, L. 2014, ApJ, 783, 98

Kirkpatrick, J. D., Looper, D. L., Burgasser, A. J., et al. 2010, ApJS, 190, 100

Kleint, L., Heinzel, P., Judge, P., & Krucker, S. 2016, ApJ, 816, 88

Koch, D. G., Borucki, W. J., Basri, G., et al. 2010, ApJ, 713, L79

Kovács, G., Bakos, G., & Noyes, R. W. 2005, MNRAS, 356, 557

Kowalski, A. F., Hawley, S. L., Wisniewski, J. P., et al. 2013, ApJS, 207, 15

Kretzschmar, M. 2011, A&A, 530, A84

Lecavelier des Etangs, A., Bourrier, V., Wheatley, P. J., et al. 2012, A&A, 543, L4

Loyd, R. O. P., France, K., Youngblood, A., et al. 2018, ApJ, 867, 71

Luger, R., Kruse, E., Foreman-Mackey, D., Agol, E., & Saunders, N. 2018, AJ, 156, 99

Lurie, J. C., Davenport, J. R. A., Hawley, S. L., et al. 2015, ApJ, 800, 95

Mann, A. W., Feiden, G. A., Gaidos, E., Boyajian, T., & von Braun, K. 2015, ApJ, 804, 64

Mann, A. W., Feiden, G. A., Gaidos, E., Boyajian, T., & von Braun, K. 2016, The Astrophysical Journal, 819, 87

Maschberger, T. & Kroupa, P. 2009, MNRAS, 395, 931

Mondrik, N., Newton, E., Charbonneau, D., & Irwin, J. 2019, ApJ, 870, 10

Morin, J., Donati, J. F., Petit, P., et al. 2008, MNRAS, 390, 567

Namekata, K., Sakaue, T., Watanabe, K., et al. 2017, ApJ, 851, 91

Nardiello, D., Libralato, M., Bedin, L. R., et al. 2016, MNRAS, 463, 1831

Olivares, J., Bouy, H., Sarro, L. M., et al. 2019, A&A, 625, A115

Olivares, J., Sarro, L. M., Moraux, E., et al. 2018, A&A, 617, A15

Paudel, R. R., Gizis, J. E., Mullan, D. J., et al. 2018, ApJ, 861, 76

Pecaut, M. J. & Mamajek, E. E. 2013, ApJS, 208, 9

Priest, E. & Forbes, T. 2002, A&A Rev., 10, 313

Queiroz, A. B. A., Anders, F., Santiago, B. X., et al. 2018, MNRAS, 476, 2556

Rayner, J. T., Cushing, M. C., & Vacca, W. D. 2009, ApJS, 185, 289

Rebull, L., Stauffer, J., Bouvier, J., et al. 2016a, Astronomical Journal, 152, 113, bibtex: 2016AJ....152..113R bibtex[eid=113;adsurl=https://ui.adsabs.harvard.edu/abs/2016AJ....152..113R;adsnote=Provided by the SAO/NASA Astrophysics Data System]

Rebull, L. M., Stauffer, J. R., Bouvier, J., et al. 2016b, AJ, 152, 113

Rebull, L. M., Stauffer, J. R., Hillenbrand, L. A., et al. 2017, ApJ, 839, 92

Reid, I. N. & Hawley, S. L. 2005, New Light on Dark Stars: Red Dwarfs, Low-Mass Stars, Brown Dwarfs, 2nd edn., Springer-Praxis books in astronomy and astrophysics (Berlin ; New York : Chichester, UK: Springer ; Praxis)

Reino, S., de Bruijne, J., Zari, E., d'Antona, F., & Ventura, P. 2018, MNRAS, 477, 3197

Sammis, I., Tang, F., & Zirin, H. 2000, ApJ, 540, 583

Schmidt, S. J. 2014, Mem. Soc. Astron. Italiana, 85, 741

Schmidt, S. J., Hawley, S. L., West, A. A., et al. 2015, AJ, 149, 158

Schmidt, S. J., Shappee, B. J., Gagné, J., et al. 2016, ApJ, 828, L22

Schmidt, S. J., West, A. A., Bochanski, J. J., Hawley, S. L., & Kielty, C. 2014, PASP, 126, 642

Schmidt, S. J., West, A. A., Hawley, S. L., & Pineda, J. S. 2010, AJ, 139, 1808

See, V., Jardine, M., Vidotto, A. A., et al. 2017, MNRAS, 466, 1542

Shibayama, T., Maehara, H., Notsu, S., et al. 2013, The Astrophysical Journal Supplement Series, 209, 5

Shibayama, T., Maehara, H., Notsu, S., et al. 2013, ApJS, 209, 5

Skrutskie, M. F., Cutri, R. M., Stiening, R., et al. 2006, AJ, 131, 1163

Soares-Furtado, M., Hartman, J. D., Bakos, G. Á., et al. 2017, Publications of the Astronomical Society of the Pacific, 129, 044501

Tilley, M. A., Segura, A., Meadows, V., Hawley, S., & Davenport, J. 2019, Astrobiology, 19, 64

Toriumi, S., Schrijver, C. J., Harra, L. K., Hudson, H., & Nagashima, K. 2017, ApJ, 834, 56

Van Cleve, J. E., Howell, S. B., Smith, J. C., et al. 2016, PASP, 128, 075002

Vanderburg, A. & Johnson, J. A. 2014, Publications of the Astronomical Society of the Pacific, 126, 948

Vanderplas, J., Connolly, A., Ivezić, Ž., & Gray, A. 2012, in Conference on Intelligent Data Understanding (CIDU), 47 –54

Vinícius, Z., Barentsen, G., Hedges, C., Gully-Santiago, M., & Cody, A. M. 2018

Walkowicz, L. M., Basri, G., Batalha, N., et al. 2011, AJ, 141, 50

Watanabe, K., Shimizu, T., Masuda, S., Ichimoto, K., & Ohno, M. 2013, ApJ, 776, 123

West, A. A., Morgan, D. P., Bochanski, J. J., et al. 2011, AJ, 141, 97

West, A. A., Weisenburger, K. L., Irwin, J., et al. 2015, ApJ, 812, 3

Wheatland, M. S. 2004, ApJ, 609, 1134

Yang, H. & Liu, J. 2019, ApJS, 241, 29

Yang, H., Liu, J., Gao, Q., et al. 2017, ApJ, 849, 36

Yee, S. W., Petigura, E. A., & von Braun, K. 2017, ApJ, 836, 77

Appendix A: Membership probabilities

To match catalogs on RA and declination we used the `astroML.crossmatch` tool for Python (Vanderplas et al. 2012). For the studies with classifiers we assigned membership probabilities as follows. In Gonzalez (2016):

$$
\begin{aligned}
p(M(\text{member})) &= 0.9, \\
p(BM(\text{binary member})) &= 0.9, \\
p(N(\text{non-member})) &= 0.1, \\
p(SN(\text{single non-member})) &= 0.1, \\
p(BN(\text{binary non-member})) &= 0.1, \\
p(U(\text{unknown member})) &= 0.5.
\end{aligned}
$$

In Curtis et al. (2013):

$$
\begin{aligned}
p(Y(\text{highest confidence member})) &= 0.9, \\
p(P(\text{possible/probable member})) &= 0.7, \\
p(N(\text{not likely/non-member})) &= 0.7, \\
p(B(\text{photometry consistent with blue stragglers})) &= 0.0.
\end{aligned}
$$

In Rebull et al. (2017):

$$
\begin{aligned}
p((\text{best})) &= 0.9, \\
p((\text{ok})) &= 0.6, \\
p((\text{else})) &= 0.1.
\end{aligned}
$$

Members from Rebull et al. (2016a); Douglas et al. (2017); and Gaia Collaboration et al. (2018a) were assigned $p = 0.9$ if they appeared in the final catalog.

Table A.1 gives an overview over different membership catalogs. Figure A.1 shows membership probability histograms of the final sample broken down by membership source. Detailed intructions on how to reproduce the final sample of members in each cluster, and corresponding tables, Python scripts, and Jupyter notebooks can be found online[6]

Appendix B: Cluster parameters

Appendix C: Broadband photometry: quality cuts and conversions

We required `flux/flux_error` $\geq$ 10 for Gaia G, BP, and RP bands. We require that the 2MASS measurements for J, H, and K to be "A". "A" means that measurements had $S/N > 10$ and $\sigma < 0.11$. For PanSTARRS photometry, we required that the `QF_OBJ_GOOD` quality filter flag was set.
SDSS and PS1 *ugrizy* bands are similar but not identical, but can be converted using Table 2 in Finkbeiner et al. (2016).

Appendix D: Pixel saturation

Resolve different levels of pixel saturation (>1, >10) and how they contribute to the deviations from the single power law at the highest energies.

---

[6] `https://github.com/ekaterinailin/`
`flares-in-clusters-with-k2-ii`

Appendix E: Solar system objects

Solar system objects (SSOs) produce brightness excursions in K2 light curves that can closely resemble flare signatures. Often, they can be distinguished by their symmetric rise and decay shape as contrasted with the typical fast-rise gradual decay flare shape (Davenport et al. 2014). M. H. Christiansen and colleagues developed a routine called `SkyBoT` that matches positions and times to passages of SSOs listed in YYY. RA, declination, start, stop, and mid epochs of flares in BKJD are the input parameters. We excluded all flare candidates that occurred within X minutes of a SSO passage at the star's position. This procedure removed ZZ% of all flare candidates. In the case of high energy flares, we confirmed the passage by manually inspecting the pixel file with the `lightkurve interact` function for TargetPixelFiles.

Appendix F: Universality of power law exponent α

We compiled a exhaustive (?) table of previous work where power laws were fitted to FFDs using different methods. Table F.1 lists the overview. While particular studies consistently find values above or below $\alpha \approx 2$, the comparison of different studies points towards unresolved systematic errors in all these studies.

Appendix G: Expanding the likelihood

The rate λ_2 of flares with energies larger than S_2 is given in Wheatland (2004) as

$$
\lambda_2 = \lambda_1 \cdot \left(\frac{S_1}{S_2}\right)^{\alpha-1}. \tag{G.1}
$$

S_1 denotes the energy above which all flares are detected. λ_1 is the corresponding rate. α remains the power law exponent of the flare frequency distribution.
We are also given the posterior distribution for the rate λ_2 of flares above S_2 in Eq. (20) in Wheatland (2004):

$$
\begin{aligned}
P_2(\lambda_2) &= \int_1^\infty \mathrm{d}\alpha \int_0^\infty \mathrm{d}\lambda_1 \delta\left(\lambda_2 - \lambda_1 \cdot \left(\frac{S_1}{S_2}\right)^{\alpha-1}\right) \\
&\quad \cdot P_1(\lambda_1) \cdot P_\alpha(\alpha)
\end{aligned} \tag{G.2}
$$

As we have additional information in the form of uncertainties in our data $S = \{S_i, \lambda_i, \sigma_{S,i}\}$, we can expand Eq. G.2 with this knowledge. Assuming that the observed flare energies S_i with cumulative rates λ_i are distributed around the real flare energies $S_{0,i}$ with Gaussian uncertainties $\sigma_{S,i}$, we can define:

$$
\begin{aligned}
p(S_i|\lambda_1, \alpha, \sigma_{S,i}) &= \frac{1}{2\pi\sqrt{\sigma_{S,i}}} e^{-\frac{(S_i - S_{0,i})^2}{2\sigma_{S,i}^2}} \\
&= \frac{1}{2\pi\sqrt{\sigma_{S,i}}} e^{-\frac{\left(S_i - S_1\left(\frac{\lambda_i}{\lambda_1}\right)^{-1/(\alpha-1)}\right)^2}{2\sigma_{S,i}^2}}
\end{aligned} \tag{G.3}
$$

We assume in Eq. G.3 that uncertainties on λ_1 are negligible. Eq. G.2 then reads:

$$
\begin{aligned}
P_2(\lambda_2) &= \int_1^\infty \mathrm{d}\alpha \int_0^\infty \mathrm{d}\lambda_1 \delta\left(\lambda_2 - \lambda_1 \cdot \left(\frac{S_1}{S_2}\right)^{\alpha-1}\right) \\
&\quad \cdot P_1(\lambda_1) \cdot P_\alpha(\alpha) \cdot P_S(S|\lambda_1, \alpha, \sigma_S)
\end{aligned} \tag{G.4}
$$

Table A.1. Membership catalogs overview. No distance are given for Hyades we adopted individual distances for all members.

source	type	clusters covered	notes
Curtis et al. (2013)	classifier	Rup 147	
Douglas et al. (2014)	probability	Hyades, Praesepe	meta study
Gonzalez (2016)	classifier	M67	
Rebull et al. (2016a)	members list	Pleiades	meta study
Rebull et al. (2017)	classifier	Praesepe	meta study
Douglas et al. (2017)	members list	Praesepe	meta study
Gaia Collaboration et al. (2018a)	members list	Hyades, Rup 147, Pleiades, Praesepe	Gaia DR2, (1)
Cantat-Gaudin et al. (2018)	probability	Rup 147, Pleiades, Praesepe	Gaia DR2
Gao (2018)	probability	M67	Gaia DR2
Reino et al. (2018)	probability	Hyades	Gaia DR1, (1)
Olivares et al. (2018)	probability	Pleiades	Gaia DR2, DANCe
Olivares et al. (2019)	probability	Rup 147	Gaia DR2, DANCe

Notes. DANCe: DANCe membership study project. (1) Positions for Hyades were propagated to epoch 2000 using Gaia proper motions.

with

$$P_S(S|\lambda_1, \alpha, \sigma_S) = C \prod_{i=1}^{M} p(S_i|\lambda_1, \alpha, \sigma_{S,i}). \tag{G.5}$$

C absorbs the normalization, or evidence term.
Following Wheatland (2004), we marginalize over λ_1 using the δ function in G.4 to obtain
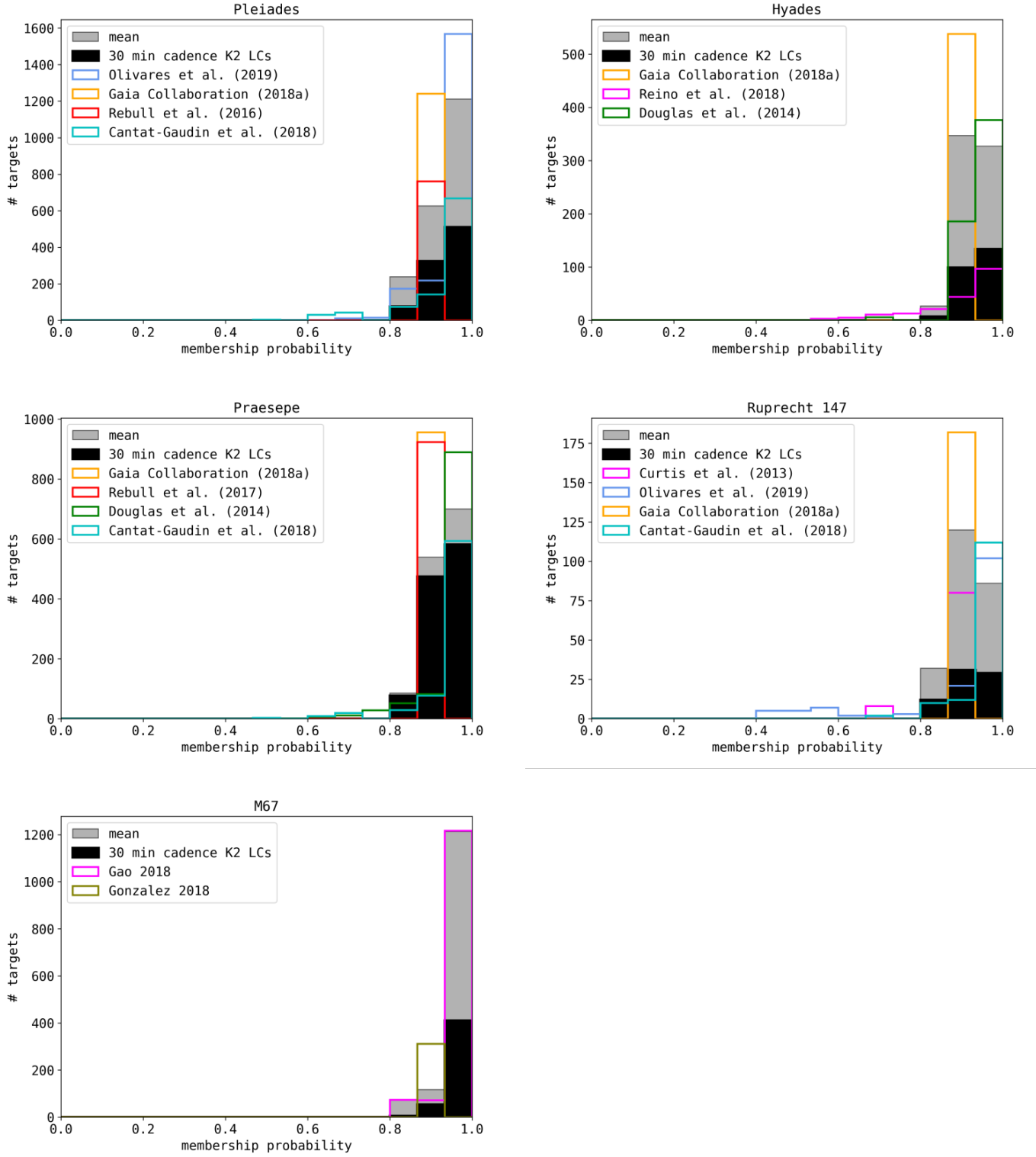
$$P_2(\lambda_2) = \int_1^\infty d\alpha \cdot P_1\left(\lambda_2 \cdot \left(\frac{S_2}{S_1}\right)^{\alpha-1}\right) \cdot P_\alpha(\alpha)$$

$$\cdot P_S\left(S|\lambda_2 \cdot \left(\frac{S_2}{S_1}\right)^{\alpha-1}, \alpha, \sigma_S\right) \tag{G.6}$$

Transforming P_S into a function of ϵ with $\lambda_1 = -\ln(1-\epsilon)/\Delta T$ yields:

$$P_S(S|\epsilon, \alpha, \sigma_S) = C \prod_{i=1}^{M} p(S_i|\epsilon, \alpha, \sigma_{S,i})$$

$$= \frac{C}{\Delta T(1-\epsilon)}$$

$$\cdot \prod_{i=1}^{M} \left[\frac{1}{2\pi \sqrt{\sigma_{S,i}}} e^{-\frac{\left(S_i - S_2\left(\frac{-\ln(1-\epsilon)}{\Delta T \lambda_i}\right)^{1/(\alpha-1)}\right)^2}{2\sigma_{S,i}^2}} \right] \tag{G.7}$$

Finally, P_S enters the joint posterior distribution from Eq. 2, that becomes

$$p(\epsilon, \alpha) = C \cdot (-\ln(1-\epsilon)^M)$$

$$\cdot (\alpha-1)^M \cdot \Gamma(\alpha) \left[\frac{(S_2/S_1)^{M+1}}{\pi}\right]^\alpha$$

$$\cdot (1-\epsilon)^{(T/\Delta T) \cdot (S_2/S_1)^{\alpha-1}-1}$$

$$\cdot P_S(S|\epsilon, \alpha, \sigma_S). \tag{G.8}$$

Fig. A.1. Membership histograms.

Table B.1. Non-exhaustive literature overview over OC parameters.

cluster	source	distance [pc]	age [Myr]	[Fe/H]
Pleiades	**adopted in this work:**	135.6	$135\pm^{25}_{25}$	-0.037 ± 0.026
Pleiades	Bossini et al. (2019)[a]		$86.5\pm^{6}_{2.4}$	
Pleiades	Cantat-Gaudin et al. (2018)	135.6		
Pleiades	Gossage et al. (2018)		$135\pm^{25}_{25}$	
Pleiades	Yen et al. (2018)	126.3	$141.3\pm^{170}_{100}$	
Pleiades	Chelli and Duvert (2016)	139		
Pleiades	Netopil et al. (2016)			-0.01
Pleiades	Dahm (2015)		$112\pm^{5}_{5}$	
Pleiades	Scholz et al. (2015)	130	120	
Pleiades	Conrad et al. (2014)			-0.037 ± 0.026
Pleiades	Melis et al. (2014)	136		
Pleiades	Bell et al. (2012)	135	125	
Hyades	**adopted in this work:**[c]		$690\pm^{160}_{100}$	0.13 ± 0.02
Hyades	Gaia Collaboration (2018)		$690\pm^{160}_{100}$	
Hyades	Gossage et al. (2018)		680	
Hyades	Liu et al. (2016)			±0.02
Hyades	Netopil et al. (2016)			0.13
Hyades	Taylor and Joner (2005)			0.103 ± 0.008
Hyades	Cummings et al. (2005)			0.146 ± 0.004
Hyades	Salaris et al. (2004)		650	0.15
Hyades	Perryman et al. (1998)		$625\pm^{50}_{50}$	
Hyades	Martin et al. (1998)		$650\pm^{70}_{70}$	
Praesepe	**adopted in this work:**	185.5	$750\pm^{3}_{7}$	0.16
Praesepe	Bossini et al. (2019)		$750\pm^{3}_{7}$	
Praesepe	Cantat-Gaudin et al. (2018)	185.5		
Praesepe	Gossage et al. (2018)		590	
Praesepe	Yen et al. (2018)	183	$794\pm^{253}_{269}$	
Praesepe	Netopil et al. (2016)			0.16
Praesepe	Scholz et al. (2015)	187	832	
Praesepe	Boesgaard et al. (2013)			0.12
Praesepe	Boudreault et al. (2012)	160	630	
Praesepe	Salaris et al. (2004)	175	650	
Rup 147	**adopted in this work:**	305	$2650\pm^{380}_{380}$	0.08 ± 0.07
Rup 147	Bragaglia et al. (2018)			0.08 ± 0.07
Rup 147	Cantat-Gaudin et al. (2018)	305		
Rup 147	Gaia Collaboration (2018)	309	$1995\pm^{404}_{257}$	
Rup 147	Torres et al. (2018)	283	$2650\pm^{380}_{380}$	
Rup 147	Curtis (2016)[b]			0.10 ± 0.02
Rup 147	Scholz et al. (2015)	270	1953	
Rup 147	Curtis et al. (2013)	300	$3125\pm^{125}_{125}$	0.07 ± 0.03
M67	**adopted in this work:**	908	$3639\pm^{17}_{17}$	$-0.102 \pm .081$
M67	Bossini et al. (2019)		$3639\pm^{17}_{17}$	
M67	Netopil et al. (2016)			0.03
M67	Scholz et al. (2015)		$3428\pm^{147}_{72}$	
M67	Conrad et al. (2014)			$-0.102 \pm .081$
M67	Dias et al. (2012)	908	4300	
M67	Oñehag et al. (2011)	880	4200	0.02

Notes. [a] Bossini et al. (2019) noted some caveats for their determination of ages of young clusters, for which they used Gaia DR2 photometry for isochrone fitting. [b] Curtis (2016) reanalysed HIRES spectra using an improved spectroscopic method as compared to Curtis et al. (2013). [c] We did not adopt a mean value for the Hyades distance because the cluster members are on average closer than 50 pc.

Table F.1. Literature overview over power law fitting approaches to FFDs.

Who	method	data	$\alpha - 1$
Hawley et al. (2014)	LSq with Poisson uncertainty, increase the low energy limit until the fit is robust		.95 (binned), 1.01 (cumulative)
Davenport (2016)	weighted LSq, asymmetric Poisson confidence intervals following Gehrels1986		
Gizis (2017)	de-biased MLE (Arnold2015), weight each point with sqrt(N) in each bin (Clauset+2009	22 flares on one M7 UCD	.6-1. (31-33 erg)
Paudel et al. (2018)	ML from a paper in 2010, used emcee (Foreman-Mackey2013)		
Lacy (1976)	graphical, linear LSq	386 flares on UV Cetis	.43-1.
Güdel et al.(2003)	-		
Davenport et al. (2012)	Fit $\log_{10} Y = \alpha + (\beta \log_{10} X)(10 - \gamma/(X + \delta))$	~50,000 M dwarfs from SDSS and 1321 M dwarfs from 2MASS	.9-2.1
Lurie et al. (2015)	Bayesian Markov chain Monte Carlo based algorithm (Kelly 2007) for linear regression	2 dMe5 dwarfs	.92-1.03
Audard et al. (2000)	Crawford+1970 MLE (Jauncey-style)	EUVE 12 F-M type stars, 10-20 flares each	.46-1.61
Shakhovskaia (1989)	linear representation, power laws from Gershberg/Shakhovskaya1983	30-40 dK0-dM8, 200 flares	.4-1.4
Yang et al. (2017)	binned FFDs	103187 flares on 540 M-type dwarfs in Kepler	1.07 +/- 0.35
Howard et al. (2018)	fit a cumulative power law, MCMC for uncertainties	575 flares on 284 stars	0.84-1.34
Hilton et al. (2011)			.63-.83